J. Fluid Mech. (2014), *vol.* 738, *pp.* 299–334. © Cambridge University Press 2013
doi:10.1017/jfm.2013.594

Linear stability analysis of a shear layer induced by differential coaxial rotation within a cylindrical enclosure

Tony Vo[1], Luca Montabone[2,‡] and Gregory J. Sheard[1,†]

[1]Department of Mechanical and Aerospace Engineering, Monash University, VIC 3800, Australia

[2]Atmospheric, Oceanic and Planetary Physics, University of Oxford, Parks Road, Oxford OX1 3PU, UK

(Received 9 June 2013; revised 26 September 2013; accepted 4 November 2013;
first published online 5 December 2013)

The generation of distinct polygonal configurations via the instability of a Stewartson shear layer is numerically investigated. The shear layer is induced using a rotating cylindrical tank with differentially forced disks located at the top and bottom boundaries. The incompressible Navier–Stokes equations are solved on a two-dimensional semi-meridional plane. Axisymmetric base flows are consistently found to reach a steady state for a wide range of flow conditions, and details of the vertical structure are revealed. An axially invariant two-dimensional flow is ascertained for small $|Ro|$, which substantiates the Taylor–Proudman theorem. Sufficient increases in $|Ro|$ forcing develops flow features that break this quasi-two-dimensionality. The onset of this breaking occurs earlier with increasing $|Ro|$ for $Ro > 0$ compared with $Ro < 0$. The thickness scaling of the vertical Stewartson layers are in agreement with previous analytical results. Growth rates of the most unstable azimuthal wavenumber from a global linear stability analysis are obtained. The threshold between axisymmetric and non-axisymmetric flow follows a power law, and both positive- and negative-Ro regimes are found to adopt the same threshold for instability, namely $|Ro| \geqslant 18.1E^{0.767}$. This relationship corresponds to a constant critical internal Reynolds number of $Re_{i,c} \simeq 22.5$. A review of reported critical internal Reynolds number and their characteristic length scales yields a consistent instability onset given by $|Ro|/E^{3/4} = 15.4$–16.6; here we find $|Ro|/E^{3/4} = 15.8$. At the onset of linear instability, the initially circular shear layer deforms, resulting in a polygonal structure consistent with barotropic instability. Dominant azimuthal wavenumbers range from 3 to 7 at the onset of instability for the parameter space explored. Empirical relationships for the preferential wavenumber have been obtained. Additional instability modes have been discovered that favour higher wavenumbers, and these exhibit structures localized to the disk–tank interfaces.

Key words: instability, rotating flows, shear layers

1. Introduction

Rotating flows are abundant in nature and are renowned for their instabilities leading to the formation of intriguing structures of geometric shape, for which a comprehensive understanding is desired.

† Email address for correspondence: Greg.Sheard@monash.edu

‡ Present address: Space Science Institute, Boulder, CO 80301, USA.

https://doi.org/10.1017/jfm.2013.594 Published online by Cambridge University Press

One such instability is associated with the presence of a horizontal shear layer induced by differential rotation. This region of fluid is also called a 'Stewartson layer', after the person who performed the first comprehensive theoretical study of the shear layers of a rotating flow with sharp gradients in the azimuthal velocity (Stewartson 1957). Under particular circumstances, a shear-layer instability (also called 'barotropic instability') can deform the initially axisymmetric Stewartson layer and produce non-axisymmetric, polygonal fluid patterns. These geometric patterns, usually non-stationary with respect to the rotating background flow, can be visualized as regular arrays of vorticity patches, or even stretched coherent vortices. Stewartson layers and associated barotropic instability are considered common features of many types of fluid flows, with range of scales that vary greatly from laboratory experiments through to geophysical and astrophysical systems. Some examples at laboratory scale include experiments from Hide & Titman (1967), Niino & Misawa (1984), Solomon, Holloway & Swinney (1993), Früh & Read (1999), van de Konijnenberg *et al.* (1999) and Aguiar *et al.* (2010). Intriguingly, even laboratory experiments with free surface fluids at the interface with a partially dry rotating solid bottom exhibit shear-layer instability capable of producing a non-axisymmetric interfacial pattern, characterized by polygonal shapes (Vatistas 1990; Jansson *et al.* 2006). Geophysical examples include the possible formation of regular arrays of meso-vortices within strongly sheared flows inside the eye of a hurricane (e.g. Kossin & Schubert 2001, 2004). Geometric patterns are also observed in the morphology of planetary polar vortices, and barotropic instability of the circumpolar jet is often put forward as a hypothesis for their formation. A good example is the hexagonal structure observed by *Voyager* and *Cassini* spacecraft at the north pole of Saturn (Godfrey 1988; Fletcher *et al.* 2008), while a hurricane-like eyewall structure is observed at the south pole (Dyudina *et al.* 2009). The work by Aguiar *et al.* (2010) exemplifies the dynamical similarities between Saturn's northern polar vortex and the flow structure produced in a differential-disk rotating apparatus. Venus is another example where geometric patterns can be observed in the morphology of both northern (Murray, Wildey & Westphal 1963; Taylor *et al.* 1979) and southern polar vortices (Piccioni *et al.* 2007; Luz *et al.* 2011), and barotropic instability has been considered (Limaye *et al.* 2009). Finally, there exist examples of instability of a shear layer at astrophysical scales as well. Gilman & Fox (1997) have generalized the problem of barotropic instability on a sphere to its hydromagnetic analogue by demonstrating that the differential rotation of the solar photosphere is unstable when a non-uniform toroidal magnetic field is added. Peralta *et al.* (2009) have presented numerical simulations of a superfluid Stewartson layer in the outer core of a differentially rotating neutron star. The nonlinear instability of Stewartson layers can even relate to Keplerian accretion disks, as discussed in § 2.

Thus, understanding the underlying instabilities in these rotating flows may provide deeper insight into the origins of the natural polar vortices and other geophysical phenomena. Such flows have been reproduced in simple rotating container configurations and have illustrated excellent dynamical similarity across a wide range of scales (e.g. Montabone *et al.* 2010*b*). This has generated interest in understanding the fundamental dynamics of these flow systems.

Shear layers emerging in rotating systems are best studied in the laboratory. The generation of differentially rotating layers of fluid can be easily obtained by mechanical forcing. Rotating disks/bottom experiments (e.g. Hide & Titman 1967; Früh & Read 1999; van de Konijnenberg *et al.* 1999) and source–sink experiments (e.g. Sommeria, Meyers & Swinney 1991; Montabone *et al.* 2010*a*) are two of the most common techniques used to investigate the barotropic instability of shear layers.

https://doi.org/10.1017/jfm.2013.594 Published online by Cambridge University Press

Although the appearance of polygonal patterns and arrays of vortices has mostly been described in experiments with mechanically rotating parts, recent source–sink studies have successfully shown that such structures can readily develop from barotropically unstable jets (Montabone *et al.* 2010*b*; Vo, Sheard & Montabone 2011). Simple two-dimensional numerical models have also captured the essential features of these vortical structures (van de Konijnenberg *et al.* 1999; Früh & Nielsen 2003).

The aim of this study is to numerically investigate the stability of flows produced via a differentially rotating disk set-up closely related to Stewartson's (1957) theoretical work and the experimental work of Früh & Read (1999). This will provide insight into the axisymmetric structure of the flow, the degree of depth independence, and the non-axisymmetric stability of the flow. The system differs from the experimental set-up through the absence of a central rod used to physically drive the rotation of the disks. The presence of this rod may become significant in generating Taylor–Couette type instabilities in the flow as the container acts as an annulus. Disturbances have been observed to shed off the rod for time-dependent flow, which may interact and disrupt larger structures formed through barotropic instability. Therefore, the absence of the rod in this numerical study may avoid the creation of instabilities other than barotropic. Positive- and negative-Rossby-number flows are investigated, and the differences in their stability characteristics are analysed. The linear instability wavenumbers that develop from a flow defined by a pairing of Rossby number (Ro) and Ekman number (E) are mapped onto a Ro–E regime diagram. The numerical technique employed allows the instability mode shapes to be visualized in isolation, which is particularly difficult to achieve in the laboratory.

This paper is organized as follows. Previous studies relevant to this investigation are reviewed in § 2. Section 3 details the geometric model under investigation, the discretization of the geometry, the numerical treatment and the validation of the computational mesh. Numerical results and discussion pertaining to flow structures of axisymmetric base states and instability modes obtained via linear stability analysis are presented in §§ 4 and 5, respectively. Finally, a concluding discussion is presented in § 6.

2. Background on differential rotation experiments

The system considered in this paper involves a pair of disks used to drive fluid in the inner radial core of the container at a different speed to fluid in the outer region, leading to the development of a cylindrical shear layer at the interface between these differentially rotating regions. Stewartson (1957) has identified and quantified the thicknesses of the vertical shear layers in this type of flow. The Ekman layers, on the other hand, are viscous boundary layers that arise due to the friction between the bulk rotation of the flow and the rotating disks. Their thicknesses are typically given by $\delta = E^{1/2}H$, where H is an appropriate vertical length scale. Outside of the Ekman layer, the flow adopts geostrophic properties, characterized by a balance between the pressure forces and Coriolis forces. Two scalings have been found to describe the shear layers at the interface between the inner and outer fluid regions, which have come to be known as Stewartson layers. A layer with thickness scaling with $E^{1/4}$ acts to smooth out the discontinuity in angular velocity across the shear layer, while a layer with thickness scaling with $E^{1/3}$ is required to complete the meridional circulation in the region.

Beyond a critical threshold, the Stewartson layers become susceptible to barotropic instability, which manifests as a wavy structure in the azimuthal direction. The

https://doi.org/10.1017/jfm.2013.594 Published online by Cambridge University Press

threshold has been observed to be dependent on the system geometry and the controlling parameters Ro, E and Reynolds number Re (Hide & Titman 1967; Niino & Misawa 1984; Früh & Read 1999). In an unstable flow, these wave-like perturbations grow. With the contribution of nonlinear effects, these perturbations may deform the shear layer into multiple vortices that arrange themselves into a polygonal chain encircling the rotational axis. The number of vortices, and thus the resulting flow structure, have been mapped against possible governing parameters such as the Rossby number and Ekman number (Hide & Titman 1967; Aguiar *et al.* 2010) and the Reynolds number (Chomaz *et al.* 1988; van de Konijnenberg *et al.* 1999; Früh & Nielsen 2003). Previous studies have demonstrated successive transitions to lower unstable wavenumbers with increasing Rossby number and Reynolds number.

Hide & Titman (1967) investigated a differentially rotating disk submerged in a rotating tank for $|Ro| \ll 1$. When the flow loses its axisymmetry, a circular shear layer evolves on the edge of the rotating disk. This detached shear layer develops into azimuthal instability modes with wavenumbers between 2 and 6 for positive Ro. In contrast, flow patterns at negative Rossby numbers developed an off-axis ellipse rather than experiencing wave-like disturbances. Despite the differences in the resulting flow between positive and negative Ro, the transition point from axisymmetric to non-axisymmetric flow occurred at similar absolute values of Rossby number, irrespective of its sign. It should be noted that only three flow conditions in the negative-Ro regime were investigated in determining the critical Ro. The empirical fit they found for the stability threshold of critical Ro as a function of E is given by $|Ro_c| = 16.8E^{0.568}$. The resulting wavenumbers decreased as the Rossby number increased and showed little dependence on E. The trend of either decreasing Ro or Re with increasing wavenumber has been seen in many previous studies. However, linear stability results from Niino & Misawa (1984) using a quasi-geostrophic approximation suggest an increase in wavenumber with increasing Re. Decreasing E has also demonstrated a succession to lower wavenumbers.

Früh & Read (1999) investigated a very similar set-up to that studied here and produced regime diagrams for the Ro–E parameter space for positive and negative Ro. They found that the stability threshold did not strongly depend on the sign of Ro, and polygonal configurations were seen for positive and negative Ro. The empirical relationship they found for the stability threshold was $|Ro_c| \approx 27E^{0.72\pm0.03}$. The flow types differed slightly between the two Ro regimes. This is in contrast with Hide & Titman (1967), who observed major flow structure differences between positive and negative Ro.

An investigation on the discrepancy between the two experiments was conducted by Hollerbach (2003). It was concluded that the cause of the flow state anomaly observed between positive and negative Ro in Hide & Titman (1967) was due to the geometry of the system. The numerical results of flow inside a spherical shell in rapid rotation suggested that, if the fluid depth does not change or changes gradually over the shear layer, then flow states for positive and negative Ro are expected to be the same. However, if the depth abruptly changes across the shear layer as in the case of Hide & Titman (1967), then wavenumbers observed in positive- and negative-Ro cases will differ. In other words, the positive- and negative-Rossby-number stability behaviours are expected to be the same if the differentially rotating surface is mounted flush with the surrounding enclosure similar to that of Früh & Read (1999). It should also be mentioned that Aguiar & Read (2006) conducted experiments on multiple configurations for which the fluid depth abruptly increases or decreases across the shear layer with increasing radius. Despite the abrupt changes in height across the

https://doi.org/10.1017/jfm.2013.594 Published online by Cambridge University Press

Stewartson layer, only a weak asymmetry in the resulting wavenumber was found with respect to the sign of Ro. It was thought that the thickness of the disk may be the cause of the strong asymmetry observed by Hide & Titman (1967). Although experiments with a thicker disk were able to obtain an asymmetry in wavenumbers for negative and positive Ro, the large differences observed by Hide & Titman (1967) were not reproducible by Aguiar (2008).

Previous numerical investigations have been able to capture the qualitative trends observed in the experiments. The flow fields have been primarily modelled by the quasi-geostrophic equation in a two-dimensional domain, which allows very small Ekman numbers to be computed. Although these tend to capture the same dynamical features observed experimentally, they are unable to generate the entire variety of flow states, nor examine the vertical structure of the flow when two-dimensionality is broken. Also, quasi-geostrophic theory only considers the $E^{1/4}$ layer and neglects the $E^{1/3}$ layer. It has been suggested that discrepancies between numerical and experimental results may be due to the absence of this $E^{1/3}$ layer. This deficiency would be overcome by simulating three-dimensional flows.

An on-going debate in astrophysics concerns the stability of astrophysical disks that adopt a Keplerian rotation, namely $\Omega \propto r^{-3/2}$. The Keplerian velocity profile is linearly stable according to the Rayleigh–Kuo criterion (described in § 3.5) and the laminar aspect of the flow is not sufficient to cause accretion. The observed rates of angular momentum transport may be related to a nonlinear mechanism of the flow. Several experiments have employed multiple split rings, each rotating independently, to produce a Keplerian profile. This configuration is similar to the set-up studied in this paper. Provided enough rings are used, a smooth angular velocity profile can be obtained as each Stewartson layer merges to fill the entire tank. A numerical study by Hollerbach & Fournier (2004) at small Ro suggested that the influence of the Stewartson layers at each split disk and the end effects are practically unavoidable for small E. This was supported by the numerical work of Avila (2012), who noted that current split-ring configurations demonstrate turbulent flow at moderate Reynolds numbers. Recent experiments (Paoletti & Lathrop 2011; Paoletti *et al.* 2012) demonstrated finite-amplitude instabilities in a container with independent rotating cylinders. This is in contrast to the experimental results of Ji *et al.* (2006) and Schartman *et al.* (2012), who observed no such instabilities even at very large Reynolds numbers. Thus, there still remains the question as to whether a truly Keplerian flow would be unstable. Although this paper does not attempt to solve this problem directly, as only linear stability is considered, the presented results may provide some insight into this issue.

3. Methodology

3.1. *System description*

The system studied in this paper comprises a cylindrical container, rotating at angular velocity Ω, with flow variation imparted by the differential rotation of disks occupying the inner radial half of the base and lid of the container. This system is illustrated in figure 1, which identifies the key length scales and boundary conditions. The closed cylindrical tank has a radius R_t and height H. Two disks of radius R_d are centred at the top and bottom boundaries, which align with the axis of rotation of the tank. The tank and disks rotate independently at rates of Ω and $\Omega + \omega$, respectively, relative to the laboratory reference frame. The proportions of the tank are scaled to match the set-up employed by Früh & Read (1999), which had $R_t = 30$ cm, $R_d = 15$ cm

https://doi.org/10.1017/jfm.2013.594 Published online by Cambridge University Press

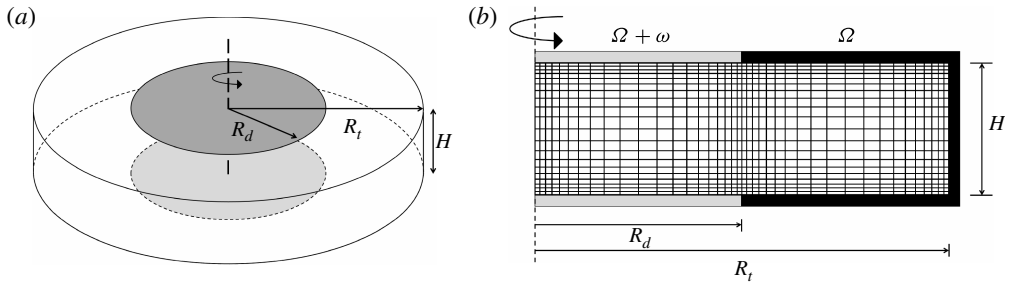


FIGURE 1. (*a*) A schematic diagram of the differential rotating disk set-up under investigation. The key dimensions are the disk radius R_d, tank radius R_t and tank height H. (*b*) The spatially discretized semi-meridional mesh used for the numerical simulations is illustrated. The disks (grey) and tank (black) rotate about the central axis (dashed line) at a rate of $\Omega + \omega$ and Ω, respectively.

and $H = 10$ cm. A schematic diagram of the model is given in figure 1(*a*). The tank is entirely filled with a working fluid that is assumed to be incompressible, Newtonian and characterized by the kinematic viscosity $\nu = \mu/\rho$, where μ is the dynamic viscosity and ρ is the fluid density. The ratio of the magnitude of the forcing to background rotation is represented by the Rossby number, *Ro*, which relates inertial to Coriolis forces in the flow. A small-Rossby-number flow indicates a high importance of Coriolis effects. For values of *Ro* much less than unity, the Taylor–Proudman theorem states that the flow is two-dimensional and invariant in the direction parallel to the axis (see Pedlosky 1987). In general, as *Ro* increases above unity, the depth independence of the flow is lost and the effects of centrifugal forces become significant. A secondary parameter used to characterize the rotating flow is the Ekman number, *E*, which represents the balance between viscous and Coriolis effects. The Rossby number and Ekman number are defined as

$$Ro = \frac{R_d \omega}{2\overline{\Omega} H} \tag{3.1}$$

and

$$E = \frac{\nu}{\overline{\Omega} H^2}, \tag{3.2}$$

where $\overline{\Omega} = \Omega + \omega/2$ is the appropriate mean rotation rate determined following Früh & Read (1999).

The Rossby and Ekman numbers combine to form a Reynolds number, and the literature defines both external and internal variants differing in the choice of reference length scale. Taking a velocity scale as the velocity differential at the interface between the disk and the tank ($R_d\omega$), an external Reynolds number is defined using the tank height as a length scale, giving

$$Re = \frac{R_d \omega H}{\nu} = \frac{2Ro}{E}. \tag{3.3}$$

Conversely, an internal Reynolds number can be defined based on the thickness of the shear layer. Stewartson (1957) demonstrated that this shear-layer thickness scales with $E^{1/4}$, and Niino & Misawa (1984) implemented $(E/4)^{1/4}H$ as an expression for the thickness given a tank height H. This value was subsequently employed in Früh &

https://doi.org/10.1017/jfm.2013.594 Published online by Cambridge University Press

Read (1999) and Aguiar *et al.* (2010). In van de Konijnenberg *et al.* (1999) a parabolic base set-up was considered, though featuring a free surface, and they took the shear-layer thickness to be $E^{1/4}H$, where the omission of the factor $(1/4)^{1/4}$ accounts for the free surface acting as a reflective plane of symmetry, rendering the fluid depth in that experiment as half that of an equivalent experiment in an enclosed tank with disks above and below the fluid. Employing the length scale $L = (E/4)^{1/4}H$ provides an internal Reynolds number

$$Re_i = \frac{R_d\omega(E/4)^{1/4}H}{\nu} = \frac{\sqrt{2}Ro}{E^{3/4}}. \tag{3.4}$$

3.2. *Numerical treatment*

The flow is governed by the time-dependent incompressible Navier–Stokes equations. Scaling lengths by R_d, velocity by $R_d\Omega$, time by Ω^{-1} and pressure by $\rho(R_d\Omega)^2$ yields dimensionless equations governing momentum and mass conservation given as

$$\frac{\partial \boldsymbol{u}}{\partial t} + (\boldsymbol{u}\cdot\boldsymbol{\nabla})\boldsymbol{u} = -\boldsymbol{\nabla}P + \frac{A^2E}{1-ARo}\nabla^2\boldsymbol{u}, \tag{3.5a}$$

$$\boldsymbol{\nabla}\cdot\boldsymbol{u} = 0, \tag{3.5b}$$

where $\boldsymbol{u} = (u_r, u_\theta, u_z)$ is the velocity vector, P is the kinematic pressure and the aspect ratio of the shear layer is given by $A = H/R_d$. In this study a cylindrical (r, θ, z) coordinate system is used.

The flow is computed on an axisymmetric meridional semi-plane that has been discretized into quadrilateral elements as shown in figure 1(*b*). The boundaries of the domain are solid and impermeable, with the exception of the left boundary. The left boundary represents the axis of rotation and spatial symmetry, and its boundary condition treatment is as per Blackburn & Sherwin (2004); zero radial and azimuthal velocities are exactly enforced as a Dirichlet boundary condition, whereas a zero Neumann condition is imposed on the axial velocity. The remaining boundaries have azimuthal velocity profiles imposed on them to induce a split-disk forcing. A single component of velocity in the azimuthal direction of $u_\theta = r(\Omega + \omega)$ is imposed on the disks, while $u_\theta = r\Omega$ is imposed on the tank walls. The mesh density is concentrated in areas where shear layers are expected to emerge and evolve.

The Navier–Stokes equations are solved in cylindrical coordinates using a nodal spectral-element discretization in space and a third-order time-integration scheme based on backward differentiation (Karniadakis, Israeli & Orszag 1991). Imposed upon each macro-element are Lagrangian tensor-product polynomial shape functions. The polynomial degree N_p is varied to control spatial resolution and is interpolated at the Gauss–Lobatto–Legendre quadrature points. The cylindrical formulation of the solver employed here has been validated in previous studies (Sheard & Ryan 2007; Sheard 2009).

3.3. *Linear stability analysis technique*

Interest in the developing non-axisymmetric three-dimensional structures on an underlying axisymmetric base flow motivates an application of a linear stability analysis. The velocity and pressure fields are decomposed into the sum of an axisymmetric field $(\overline{\boldsymbol{u}}, \overline{P})$ and a small perturbation field $(\boldsymbol{u}', P')$. As with Blackburn, Marques & Lopez (2005) and Cogan, Ryan & Sheard (2011), the perturbation field was constructed as a single complex Fourier mode of an azimuthal expansion of the flow field to accommodate the swirling precession of the flow, and the wavenumber

https://doi.org/10.1017/jfm.2013.594 Published online by Cambridge University Press

of the perturbation is a parameter in the stability analysis. Substituting these into (3.5) and eliminating terms satisfying (3.5) for axisymmetric flow as well as products of perturbation quantities yields the linearized Navier–Stokes equations

$$\frac{\partial \boldsymbol{u}'}{\partial t} + (\bar{\boldsymbol{u}} \cdot \boldsymbol{\nabla})\boldsymbol{u}' + (\boldsymbol{u}' \cdot \boldsymbol{\nabla})\bar{\boldsymbol{u}} = -\boldsymbol{\nabla} P' + \frac{A^2 E}{1 - ARo}\boldsymbol{\nabla}^2 \boldsymbol{u}', \tag{3.6a}$$

$$\boldsymbol{\nabla} \cdot \boldsymbol{u}' = 0. \tag{3.6b}$$

A linear stability analysis (Barkley & Henderson 1996) is performed to calculate the complex Floquet multipliers μ_F of the system. The Floquet multipliers correspond to the dominant eigenvalues of an evolution operator associated with time integration of the linearized Navier–Stokes equations, and are related to the exponential growth rate of individual wavenumbers through

$$\mu_F = \mathrm{e}^{\sigma T}, \tag{3.7}$$

where σ denotes the complex growth rate and T is the time interval over which the equations are integrated within the eigenmode solver. The growth rates reported later in this paper are the real component of this complex growth rate, evaluated from $\sigma_R = \log|\mu|/T$. For simplicity the subscript 'R' is omitted hereafter. Typically, T is an oscillation period, but in the case of steady-state base flows, such as are produced in the present study, T may be arbitrarily chosen. Thus a stable flow is characterized by $|\mu_F| < 1$ and an unstable flow having $|\mu_F| > 1$, with the respective growth rates being negative and positive. Eigenvectors corresponding to the leading eigenvalues (Floquet multipliers) give the mode shape of the instability on the perturbation field. The present implementation in cylindrical coordinates follows work by Sheard, Thompson & Hourigan (2005), and was recently validated by Cogan *et al.* (2011). An implicitly restarted Arnoldi method is used to extract the leading eigenmodes of the linearized perturbation fields (Sheard 2011).

3.4. *Grid independence*

To ensure grid independence, the convergence of several global parameters has been computed. A reference case featuring a small $E = 8.33 \times 10^{-5}$ and a constant $Ro = -0.833$ is considered. This case is representative of the limit of feasible computational resource usage, as smaller E produces thinner shear layers, requiring higher resolution. Thus achieving grid independence for this case ensures solution accuracy for higher E cases.

Three measures for convergence are adopted: the integral of the azimuthal velocity relative to the tank ($u_{\theta,rel} = u_\theta - \Omega r$) across the domain, the leading eigenvalue magnitude obtained by linear stability analysis of a perturbation with azimuthal wavenumber $k = 12$, and the L_2 norm taken as the integral of the velocity magnitude throughout the domain. The values are obtained once the flow has reached a steady state. The relative percentage error ε against a high-resolution reference case with element polynomial degree $N_p = 14$ is plotted in figure 2. The results demonstrate a decreasing error with increasing N_p. A threshold criterion of order $O(0.1\%)$ is sought to ensure that solution error due to finite spatial resolution is much smaller than likely laboratory sources of error. This is approximately satisfied with $N_p = 11$, which is used hereafter.

3.5. *Rayleigh–Kuo criterion for barotropic instability*

In geophysical applications, atmospheric and oceanic motions are under the influence of non-uniform background vorticity. The non-uniformity of the background vorticity

https://doi.org/10.1017/jfm.2013.594 Published online by Cambridge University Press

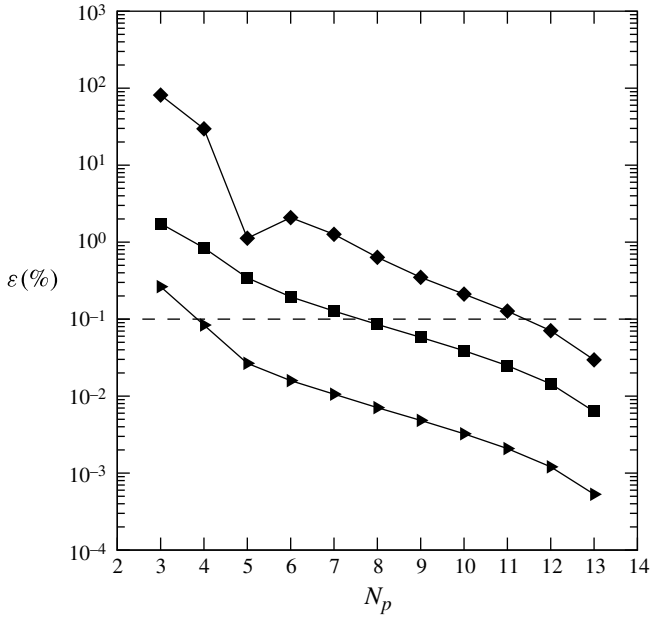


FIGURE 2. The relative percentage error ε in the global variables of the integral of the relative azimuthal velocity (squares), L_2 norm (triangles) and the leading eigenvalue magnitude (diamonds) of the case study $(Ro, E) = (-0.833, 8.33 \times 10^{-5})$. A decreasing trend with increasing polynomial degree N_p is seen with all variables. An error of $\varepsilon = 0.1\,\%$ is marked by the horizontal dashed line.

arises from the planetary rotation and the spherical shape of the planet. Thus, the vertical component of the background vorticity varies with latitude, which is measured by the Coriolis parameter $f = 2\Omega \sin\theta$, where θ is the latitude. The f-plane approximation is satisfied when f is constant, which is dynamically similar to a rotating flow of constant depth. For systems of linearly varying depth, an extra term is included in the approximation of the Coriolis parameter, known as the β-plane approximation.

A necessary condition for three-dimensional instability in barotropic two-dimensional flows was developed by Rayleigh (1880) for the f-plane and extended by Kuo (1949) for the β-plane. The condition is given by

$$\frac{\partial^2 \bar{u}}{\partial y^2} - \beta = 0, \tag{3.8}$$

where β represents the variation of the Coriolis parameter with latitude, $\bar{u}$ is the base flow velocity profile and y the northward coordinate. The condition is that the horizontal gradient of the absolute vorticity changes sign somewhere in the domain, which is represented by the terms on the left-hand side. The absolute vorticity is the sum of the background and relative vorticity. The Rayleigh–Kuo condition is a necessary but not sufficient criterion for instability.

The equivalent condition in cylindrical coordinates for a flow governed only by u_θ is

$$\frac{\partial \omega_z}{\partial r} = \frac{\partial^2 u_\theta}{\partial r^2} + \frac{1}{r}\frac{\partial u_\theta}{\partial r} - \frac{u_\theta}{r^2} - \frac{\partial f}{\partial r} = 0, \tag{3.9}$$

https://doi.org/10.1017/jfm.2013.594 Published online by Cambridge University Press

where f is the Coriolis parameter and ω_z is the axial component of vorticity. In the f-plane case as considered here, the last term $(\partial f/\partial r)$ vanishes.

4. Results: axisymmetric flow

4.1. *Axisymmetric flow structure*

Steady-state solutions were obtained on the meridional semi-plane for a variety of flow conditions. Time-evolved solutions are taken to be steady-state ones when velocity variations are less than 10^{-12} between successive time steps. Simulations are largely performed for Rossby numbers between $-4.0 < Ro < 0.6$ and Ekman numbers between $5 \times 10^{-5} < E < 3 \times 10^{-3}$. Interest in atmospheric polar vortices motivates the analysis of small positive-signed Rossby numbers, and a wider range is explored in this study for its fundamental interest. Negative and positive Ro correspond to the inner disks rotating slower and faster than the tank (in the same orientation), respectively. Counter-rotation between the disks and tank is described when $Ro < -R_d/H = -1/A$.

Typical contours of the axial velocity u_z and axial vorticity ω_z are shown in figure 3. Two cases each of positive and negative Ro of $E = 3 \times 10^{-4}$ are illustrated. For positive-Ro cases, there is Ekman pumping at the disk–tank interface $(r = 1)$ where fluid is drawn radially towards the interface in the Ekman layer and is ejected axially into the interior. To replace the fluid along the horizontal boundaries, fluid from the interior is directed back into the Ekman layer on either side of the pumping region. The flow direction is reversed for negative-Ro flows. Interesting dynamics are also demonstrated at $r = 1$ in the contours of ω_z. For the smaller positive-Ro case (figure 3*a* i), the concentrated vorticity portrays significant depth independence, which is surrounded by uniform vorticity. The interior of the flow is dominated by a depth-independent azimuthal velocity field. Thus the base flow is highly two-dimensional away from the lid and base and portrays characteristics consistent with a barotropic flow. The characteristics of the base flow at small Ro are in agreement with the Taylor–Proudman theorem. Large changes in E are required to induce the same effect to the flow structure in comparison to Ro variations. Increasing E causes a larger shear-layer region to develop and also promotes depth independence, similar to decreasing Ro. In contrast, thin detached shear layers are present at very small E.

As the positive Rossby number is increased in magnitude, the flow begins to lose its depth independence. The negative-vorticity regions located at the disk–tank interface grow into strands, which are initially symmetric about the mid-depth. Eventually, the strands elongate into the flow interior and the flow loses reflective symmetry about the mid-depth. This behaviour is shown in figure 3(*a* ii). Further increases to Ro cause 'hooks' to develop at the tips of the negative vortical strands. These are represented by a strand branching back towards the horizontal boundaries from the tip of the strand. This flow feature has only been observed in low-E flows, which form thin detached shear layers. At larger E and sufficient Ro forcing, a detached negative-vorticity region is instead present at mid-depth in the shear-layer region. These distinct features, which are observed through the progression of increasing Ro, affect the linear stability of the flow. The linear stability analysis is discussed in the next section.

Unlike positive-Ro flows, increases to the magnitude of Rossby number in the negative-Ro regime do not have any significant effect on the base flow over a wide range of Ro values. The flow preserves its depth independence outside the top and bottom Ekman layers for the majority of combinations of Ro and E computed in this study. This is portrayed in the contours of $Ro = -1.0$ and $E = 3 \times 10^{-4}$ (figure 3*b* i).

https://doi.org/10.1017/jfm.2013.594 Published online by Cambridge University Press

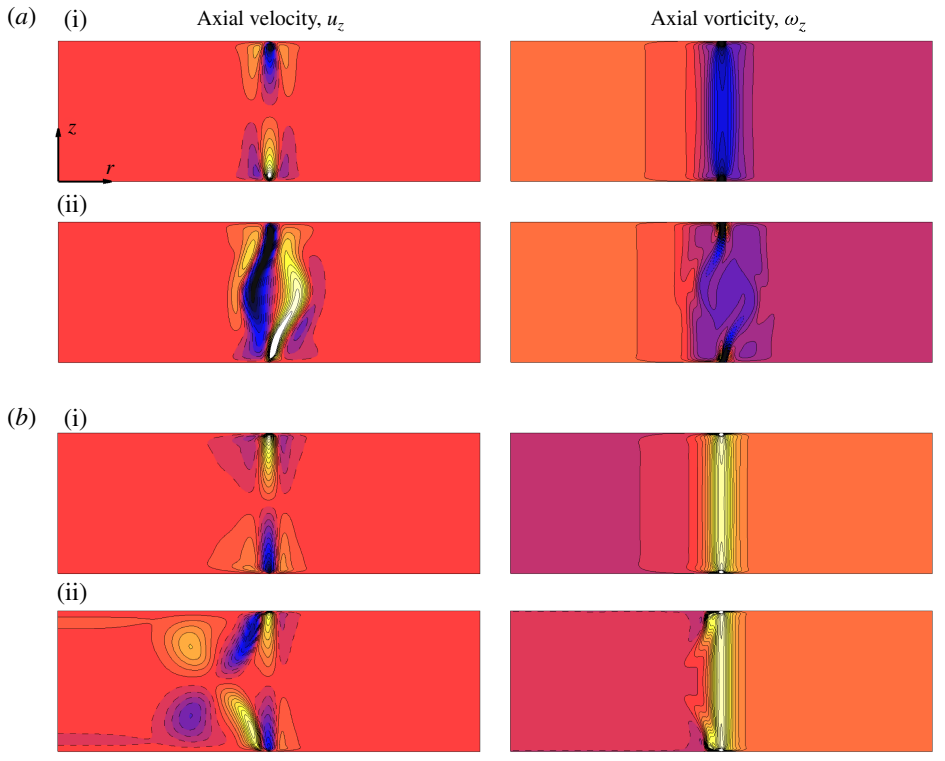


FIGURE 3. (Colour online) Structure of the axisymmetric flows visualized on the semi-meridional r–z plane. Axial velocity (left) and axial vorticity (right) are shown for $E = 3 \times 10^{-4}$ at positive and negative Ro: (a i) $Ro = 0.05$, (a ii) $Ro = 0.5$; and (b i) $Ro = -1.0$, (b ii) $Ro = -2.0$. For the axial velocity plots, equi-spaced contour levels are plotted between $\pm 0.1|Ro|(\Omega + \omega)$; while for the axial vorticity plots, equi-spaced contour levels are plotted between $2\overline{\Omega} \pm 10\omega$. Dark (blue online) and light (yellow online) contour shading represent low and high values, respectively, while solid and dashed contour lines identify positive and negative contour levels, respectively. The domain shown represents the entire semi-meridional plane with $0 \leqslant r \leqslant 2$ and $0 \leqslant z \leqslant 2/3$.

The analysis of negative-Ro cases corresponding to figure 3(a), i.e. $Ro = -0.05$ and -0.5, demonstrate qualitative features identical to figure 3(b i), although this is not shown here.

The ability of the flow to retain its axial depth dependence may be explained by the sign of the vorticity generated at the disk–tank interface. For positive-Ro flows, the decrease in angular velocity from the disk to the tank at the disk–tank interface introduces a region of negative vorticity, which develops at higher Ro. This is not observed for negative Ro, as the increase in angular velocity at the disk–tank interface produces positive axial vorticity in the vicinity. As this region is surrounded by the same-signed vorticity, it is not encouraged to grow into the interior. If this explanation holds true, the flow's two-dimensionality is expected to break if the disk and tank rotate in opposite directions. This occurs when $\omega \leqslant -\Omega$ or, equivalently, $Ro \leqslant -1/A$ ($Ro \leqslant -1.5$).

The axial velocity and axial vorticity contours for a Rossby-number flow with opposing disk and tank rotations are illustrated in figure 3(b ii). The flow condition is

https://doi.org/10.1017/jfm.2013.594 Published online by Cambridge University Press

of $Ro = -2.0$ and $E = 3 \times 10^{-4}$. Distinct features are seen in regions enclosed by the disks ($r \leqslant 1$). In addition to the vertical column of axial vorticity around $r = 1$, there are vorticity patches and strands angled towards the centre of the tank and interior of the flow originating from a point along the disk. The vorticity strand is positive, while the patch closer to the axis is negative. As the negative Rossby number increases in magnitude, the negative-vorticity patch enlarges, which forces the positive vorticity strand to incline more towards the vertical shear layer. With regards to the axial velocity, an extra circulation is seen towards the centre of the tank. However, there still remains a reflectional symmetry about $z/H = 0.5$, which is broken in the positive-Ro regime.

4.2. *Vertical shear-layer profile and thickness*

Profiles of the relative azimuthal velocity extracted at mid-depth are shown in figure 4(*a*). The profiles consistently feature three distinct regions. The two regions of linearly increasing and zero relative azimuthal velocity outside of the shear layer around $r = 1$ typify the rotation rates of the disk and tank, while the region inside the shear layer represents an interface zone over which the profiles smoothly vary from the disk to the outer tank profiles. As $|Ro|$ increases, the amplitude of the velocities increases, with the location of the peak remaining relatively constant for all $|Ro| < 0.1$ investigated. The radial position of the peak relative azimuthal velocity for larger Ro shifts closer towards the centre of the tank due to the breaking of depth independence. Decreasing E induces the same effect although the changes are less pronounced compared to Ro variations. For $|Ro| < 0.1$ the profiles are identical at other depths, excluding the vicinity of boundary layers.

The mid-depth axial vorticity profiles corresponding to the cases in figure 4(*a*) are shown in figure 4(*b*). A minimum in axial vorticity is observed at $r = 1$ for $Ro < 0.1$, with constant vorticity on either side. At the higher magnitudes of positive Ro, the vorticity profile demonstrates multiple troughs. Indeed, at these higher $|Ro|$ flows, the profiles are not depth-independent.

The radial gradients of axial vorticity for positive-Ro cases are calculated and shown in figure 4(*c*), which demonstrates $\partial\omega_z/\partial r$ changing sign at least once within the domain. The common root observed in all cases appears at $r = 1$ where the vorticity gradient changes sign, whereas it approaches zero when moving away from $r = 1$. This suggests the possibility of barotropic instability developing at the radial location of the disk–tank interface, which is explored in detail in § 5. Additional intersections of the horizontal axis are evident at higher positive Ro. Similar trends are observed for negative-Ro flows, though they are not included in the plot for clarity. The vorticity gradient consistently changes sign at $r = 1$ for small Ro, while multiple root crossings are observed at larger negative Ro.

From figure 4, it is clear that the profiles of azimuthal velocity and axial vorticity remain continuous across the disk–tank interface. The discontinuity imposed by the boundary at this interface is smoothed out via the vertical detached shear layers. Indeed, this is the role of the Stewartson layers. Theoretical analysis by Stewartson (1957) identified two nested shear layers of thicknesses scaling with $E^{1/3}$ and $E^{1/4}$ for infinitesimal Ro. The function of the thinner $E^{1/3}$ layer is to complete the meridional circulation of the Ekman pumping/suction, which in turn removes the vorticity singularity, while the role of the thicker $E^{1/4}$ layer serves to smooth out the discontinuity in angular velocity between the inner and outer sections (Smith 1984; Vooren 1992; Schaeffer & Cardin 2005).

https://doi.org/10.1017/jfm.2013.594 Published online by Cambridge University Press

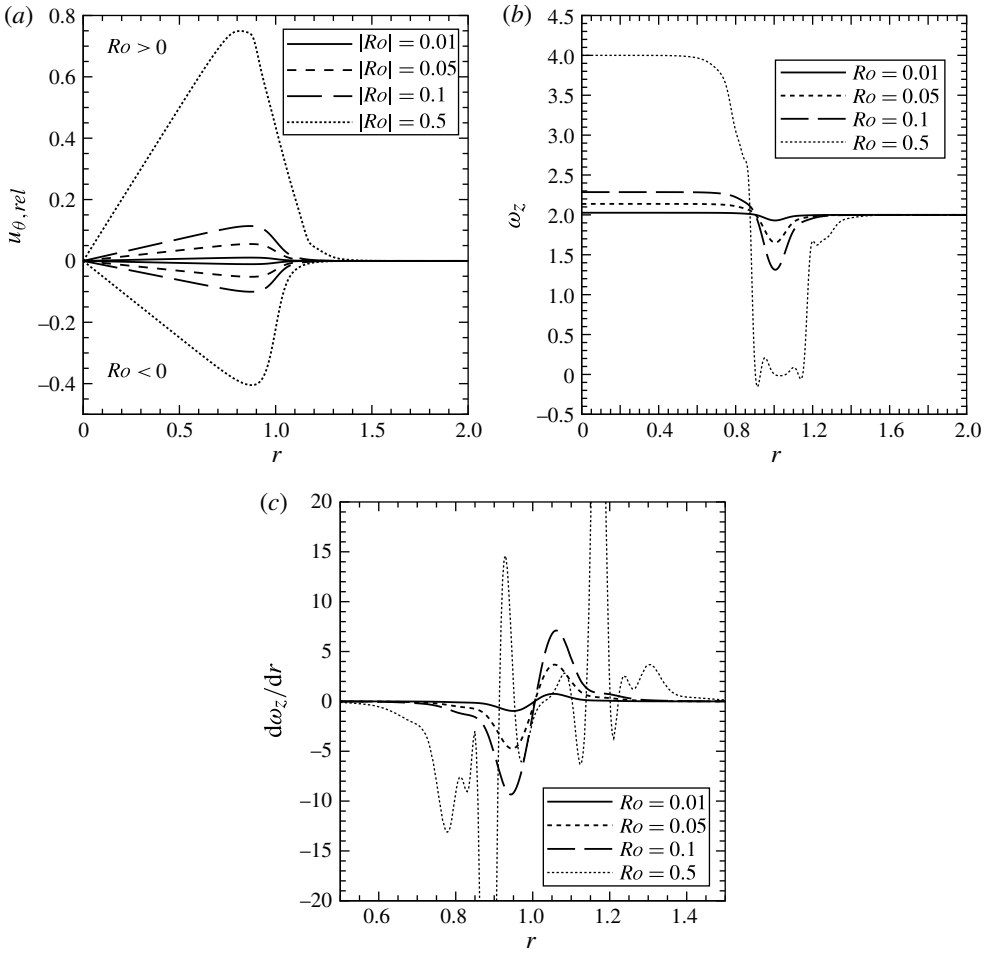


FIGURE 4. (*a*) Azimuthal velocity relative to the rotating tank against radius extracted at $z/H = 0.5$ for $E = 3 \times 10^{-4}$ at various Ro. Curves above and below the zero-line axis correspond to positive and negative Ro, respectively. (*b*) The axial vorticity profiles and (*c*) its radial gradient as a function of radius for various positive Ro only (negative-Ro data have been omitted for clarity). Root crossings of $\mathrm{d}\omega_z/\mathrm{d}r$ are observed at $r = 1$.

Aside from theoretical analysis, the only experimental investigation that has been able to retrieve a thickness scaling of the shear layers was conducted by Baker (1967). The range of Rossby numbers that Baker investigated was very small, ranging over $0.0041 < Ro < 0.038$. The scalings of the thick and thin layers were determined to be proportional to $E^{0.25\pm0.02}$ and $E^{0.4\pm0.1}$, respectively. Those scalings were determined by measuring the shear-layer thickness from measured azimuthal and axial velocity profiles, respectively, though the precise criterion used to define the edges of the shear layer is unclear. The issue of an ill-defined shear-layer edge may be the cause of a lack of numerical validation, and is further exacerbated by the frequent use of a quasi-geostrophic model, which neglects the $E^{1/3}$ layer. Additionally, there has been no mention in the literature of how the shear-layer thickness scales at higher Ro. It is evident from figure 3(*a* ii) that the theoretical scaling obtained for infinitesimal Ro breaks down at high Ro.

https://doi.org/10.1017/jfm.2013.594 Published online by Cambridge University Press

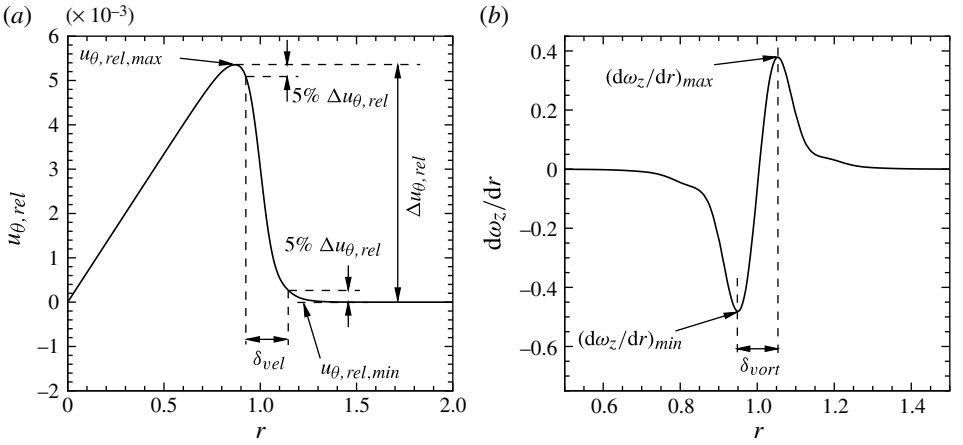


FIGURE 5. The techniques used to measure the thicknesses of (*a*) the shear layer associated with azimuthal velocity and (*b*) the shear layer associated with axial vorticity. (*a*) The relative azimuthal velocity $u_{\theta,rel}$ plotted against r. Here $\Delta u_{\theta,rel}$ is the difference between the maximum and minimum values obtained by the velocity profile at mid-depth. The thickness δ_{vel} is taken as the absolute value of the difference between the radial locations where $u_{\theta,rel}$ first reaches within 5 % of the maximum and minimum $u_{\theta,rel}$ values moving away from the disk–tank interface ($|r-1|$ increasing from zero). (*b*) The radial derivative of the axial vorticity plotted against r. The thickness δ_{vort} is taken as the absolute value of the difference between the radial locations of the maximum and minimum values of $d\omega_z/dr$ bracketing the disk–tank interface at $r = 1$.

Since the functions of the $E^{1/4}$ and $E^{1/3}$ layers are to smooth out the azimuthal velocity and axial vorticity discontinuities, respectively, it is proposed that their respective thicknesses can be determined from the profiles of azimuthal velocity and radial gradient of axial vorticity from the axisymmetric base flow. The techniques used to measure the thicknesses are illustrated in figure 5, where δ_{vel} represents the thickness of the $E^{1/4}$ layer and δ_{vort} represents the $E^{1/3}$ thickness. The thickness δ_{vel} is taken as the absolute value of the difference between the radial locations of where $u_{\theta,rel}$ first reaches within 5 % of the maximum and minimum $u_{\theta,rel}$ values on either side of the disk–tank interface ($r = 1$). Although this 5 % threshold has been chosen arbitrarily, it has been determined that the relevant results obtained through this approach are quite insensitive to the threshold value used provided that it is small (e.g. <10 %). The thickness δ_{vort} is determined by the absolute difference between the radial positions of the minimum and maximum values of $d\omega_z/dr$.

Figure 6 maps $\log_{10}\delta_{vel}$ and $\log_{10}\delta_{vort}$ on axes of $\log_{10}(E)$ and Ro. In each case a regular increase in thickness with Ekman number is observed, and additionally a continuous increase in thickness with Rossby number through both the negative and positive Rossby-number ranges is found. These plots confirm that the Stewartson layers adopt a finite thickness in the limit as $|Ro| \to 0$. This feature is not without precedent in fluid mechanics. For instance, it is well known (Schlichting 1979) that at a stagnation point in plane flow (Hiemenz flow) the boundary layer has a finite thickness at the stagnation point, despite the velocity differential across the boundary layer going to zero.

For all negative Rossby numbers (and small positive Rossby numbers), an approximately uniform vertical spacing between contour levels in both plots in figure 6

https://doi.org/10.1017/jfm.2013.594 Published online by Cambridge University Press

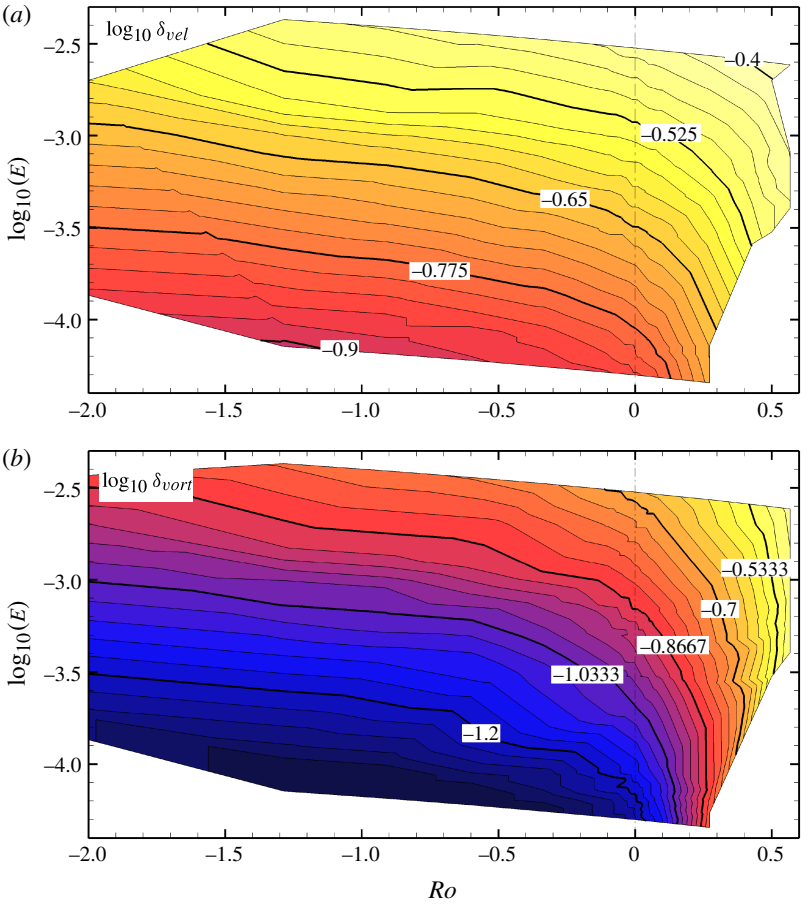


FIGURE 6. (Colour online) Contours of the base-10 logarithm of vertical shear-layer thickness plotted on axes of $\log_{10}(E)$ against Ro. Contours plots of (*a*) $\log_{10}\delta_{vel}$ and (*b*) $\log_{10}\delta_{vort}$, respectively, with thicknesses as defined in figure 5. In both plots, small to large thickness is represented by dark (blue online) to light (yellow online) contours, respectively, and thickness values take the same contour shading in both plots. Contour line intervals are 1/4 and 1/3 of the vertical axis scale in panels (*a*) and (*b*), respectively. This follows the respective expected shear-layer scalings of $E^{1/4}$ and $E^{1/3}$. The data agree with these scalings when the vertical contour line spacing matches the vertical axis tick mark spacing. The vertical dash-dotted line corresponds to the Stewartson limit of $|Ro| \to 0$, demonstrating that a finite shear-layer thickness is produced in this limit.

is seen. The contour-level spacing further indicates that the shear-layer scalings are approximately consistent with their theoretical $E^{1/4}$ and $E^{1/3}$ values. For example, power-law fits of δ_{vel} and δ_{vort} against Ekman number for a very small Rossby number ($Ro = 0.005$) yields $\delta_{vel} = 1.31E^{0.22}$ and $\delta_{vort} = 1.26E^{0.31}$, respectively. The exponents of E are in good agreement with those predicted by theory.

So why is it that an $E^{1/3}$ scaling is detected from the axial vorticity profile when Baker (1967) used the axial velocity profile to measure the $E^{1/3}$ layer? Within the Stewartson layers, fluid circulates axially towards mid-depth at positive Rossby numbers, and towards the horizontal boundaries at negative Rossby numbers.

https://doi.org/10.1017/jfm.2013.594 Published online by Cambridge University Press

Recirculation is therefore confined to one vertical half of the enclosure, and, near to mid-depth, the fluid pumped axially through the $E^{1/3}$ layer migrates horizontally near the mid-plane to complete its meridional circulation away from the Stewartson layers. The change in angular momentum as this fluid migrates radially inwards or outwards at mid-depth then modifies the axial vorticity profile, which we believe drives the detection of an $E^{1/3}$ scaling in the shear-layer thickness measured from the radial axial vorticity profile in figure 6(*b*). A similar analysis conducted on the axial velocity profiles yields an E exponent comparable to that of δ_{vort}, namely 0.31 (not shown here).

Another feature observable in figure 6 is that, at larger positive Rossby numbers, the measured thicknesses begin to lose their dependence on Ekman number (contours of constant thickness approach the vertical). This Ekman-number-independent behaviour also manifests itself in the stability of the flow to azimuthal perturbations discussed later in § 5. By inspection of the axisymmetric flows shown in figure 3 (and similar plots at other (Ro, E) pairs not shown here), it becomes apparent that this Ekman-number-independent regime corresponds to the loss of depth independence seen in the axisymmetric flows (see e.g. figure 3*a* ii).

Across the negative-Rossby-number range, the thicknesses change gradually. As Rossby numbers approach zero and increase through the range of positive values, thickness increases at an accelerating rate. This behaviour can be explained by the nonlinear relationship between differential angular velocity (ω) and Ro. While ω appears directly in the numerator of the Rossby number definition (equation (3.1)), it also enters in the denominator through the definition of $\overline{\Omega}$. Rearranging (3.1) for the normalized differential rotation gives

$$\frac{\omega}{\Omega} = \frac{2Ro}{1/A - Ro}, \tag{4.1}$$

which has an asymptotic minimum $\omega/\Omega = -2$ as $Ro \to -\infty$, and an asymptotic maximum $\omega/\Omega = \infty$ as $Ro \to 1/A$ (which corresponds to $Ro \to 1.5$ with the enclosure dimensions adopted in the present study). The similarity in Rossby-number dependence between the relationship described by (4.1) and the thickness measurements in figure 6 highlights ω/Ω as an important parameter in describing the dependence of the shear-layer thickness against Rossby number.

We now develop universal relationships for shear-layer thickness. As established from figure 6, $\delta_{vel}/E^{1/4}$ and $\delta_{vort}/E^{1/3}$ are approximately constant. When plotted against ω/Ω, linear trends were found for these normalized thickness quantities for $Ro \lesssim 0$. Least-squares fits to the data obtained the trends displayed in figure 7. These trends hold well for all negative Rossby numbers and positive Rossby numbers exhibiting depth independence in the axisymmetric flows. Once depth independence is lost, the measured shear layer becomes thicker than the universal curve, which results from the widening of the shear layer away from the lid and base as reflective symmetry across the mid-depth plane is broken (this effect can be seen when comparing panel (ii) to panel (i) in figure 3*a*).

5. Results: linear stability analysis

A linear stability analysis is used to predict the fastest-growing three-dimensional azimuthal wavenumbers that develop on the underlying axisymmetric steady-state flow, for a wide range of Ro and E. The azimuthal wavenumber is defined by $k = 2\pi/\lambda$, where λ is the angular wavelength of the instability. The zeroth

https://doi.org/10.1017/jfm.2013.594 Published online by Cambridge University Press

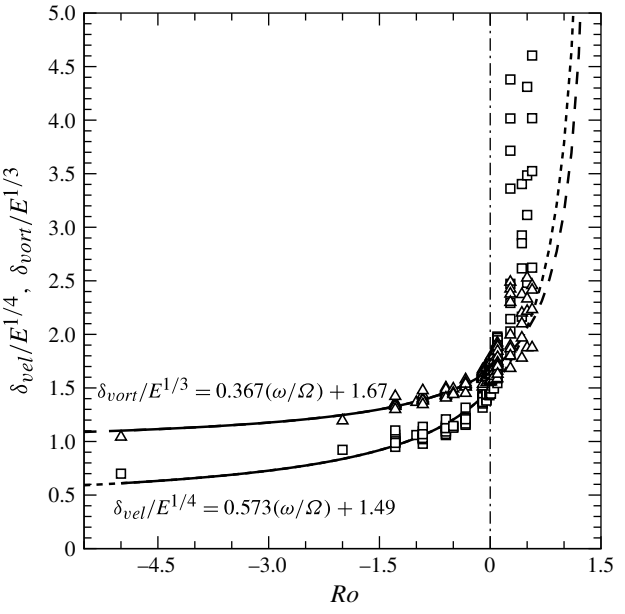


FIGURE 7. Partial collapse of the shear-layer thickness data onto universal trends as functions of E and Ro. The plot shows $\delta_{vel}/E^{1/4}$ (squares) and $\delta_{vort}/E^{1/3}$ (triangles) against Ro. Analysis determined that, while the axisymmetric flows remained depth-independent, the scaled shear-layer thicknesses varied linearly with ω/Ω. The relationships obtained from least-squares fits to the data are included on the plot. Solid lines show the Rossby-number range where the universal fits hold; and dashed lines extrapolate these fits for comparison against the data, which deviate from these trends at higher Ro.

wavenumber is omitted, as it has a synchronous nature that was found always to be stable. In contrast, the eigenvalues of non-zero wavenumbers are consistently complex, which corresponds to quasi-periodic instability modes, where the instability introduces an incommensurate frequency into the flow (Blackburn *et al.* 2005; Blackburn & Sheard 2010). In other words, the instability invokes a Hopf bifurcation from a steady axisymmetric state to an unsteady non-axisymmetric state. This analysis predicts that flows become linearly unstable under certain combinations of Ro and E. Distinct stability characteristics are observed between positive and negative Ro, which are described in §§ 5.1 and 5.2, respectively.

5.1. *Positive Rossby numbers*

5.1.1. *Growth rates*

The growth rates for a range of wavenumbers were obtained for a large number of Ro–E combinations. The fastest-growing wavenumber was established in each case, with peak unstable wavenumbers ranging primarily from 2 to 9 in the positive-Ro regime. As a comparison, unstable azimuthal modes with wavenumbers of 2–8 were typically observed in laboratory experiments (Früh & Read 1999; Aguiar *et al.* 2010).

The growth rate as a function of wavenumber for a constant small $Ro = 0.05$ for various E is shown in figure 8. A single maximum can be seen in the σ–k relationship. Local maxima typically represent distinct instability modes (e.g. Barkley & Henderson 1996). For wavenumbers beyond this maximum, the growth rate decreases monotonically. At high Ekman numbers, this peak is still present despite

https://doi.org/10.1017/jfm.2013.594 Published online by Cambridge University Press

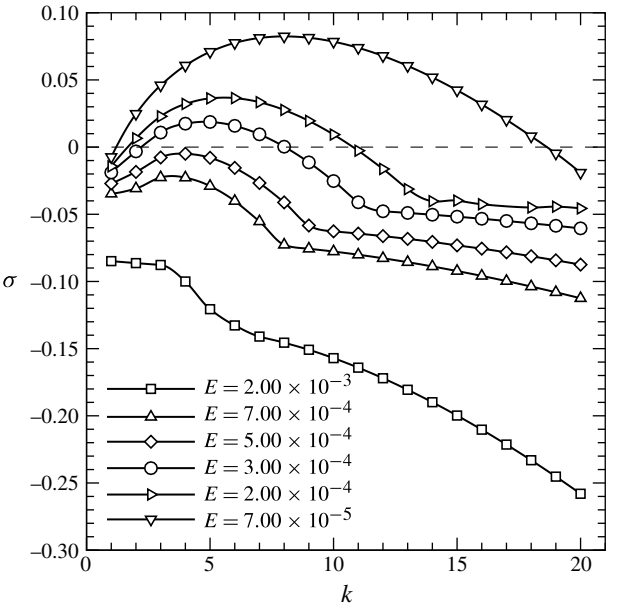


FIGURE 8. Growth rate σ as a function of azimuthal wavenumber k for various E at a low $Ro = 0.05$. The dashed line represents the zero line where points above and below symbolize stable and unstable modes, respectively.

the growth rates always remaining negative (stable flow). The flow is only unstable for low E ($< 3 \times 10^{-4}$) at $Ro = 0.05$. Several trends can be observed from this figure. The growth rates and the most unstable wavenumber increase with decreasing E. Also, the profiles do not change significantly with varying E, though the range of wavenumbers over which the mode branches are detected increases with decreasing E. For example, the mode branch covers $1 \leqslant k \leqslant 8$ for $E = 7 \times 10^{-4}$, while a larger range of $1 \leqslant k \leqslant 14$ is seen for $E = 2 \times 10^{-4}$.

Figure 9(*a*) illustrates the growth rate as a function of wavenumber at constant $Ro = 0.395$ for varying E. Similarly, with small-Ro flows, only a single mode peak comprising small wavenumbers exists for large E. This first mode peak is shown for $E = 3.16 \times 10^{-3}$ in figure 9(*a*), with the most unstable wavenumber predicted as $k_{peak} = 3$. However, unlike small-Ro flows, a second mode peak emerges at higher wavenumbers as E decreases. In fact, the emergence of the second mode peak is dependent on both Ro and E, which will be discussed in the next section. Eventually, the growth rates of these higher wavenumbers become larger than those of the first mode peak. The dominance of the second peak is shown for the case of $E = 5.26 \times 10^{-4}$, where the predicted linearly unstable wavenumber is $k_{peak} = 29$. These small-wavenumber and high-wavenumber modes will hereafter be referred to as modes I and II, respectively. A third mode peak (mode III) has also been observed, which comprises intermediate wavenumbers between modes I and II, as shown in figure 9(*b*). This third peak arises by further decreasing E or increasing Ro, and in a small number of small-E/high-Ro cases it was seen to achieve growth rates exceeding those of mode I.

The emergence of these three mode peaks may be related to the features exhibited in the base flow. Base flows on which mode I dominates are typically two-

https://doi.org/10.1017/jfm.2013.594 Published online by Cambridge University Press

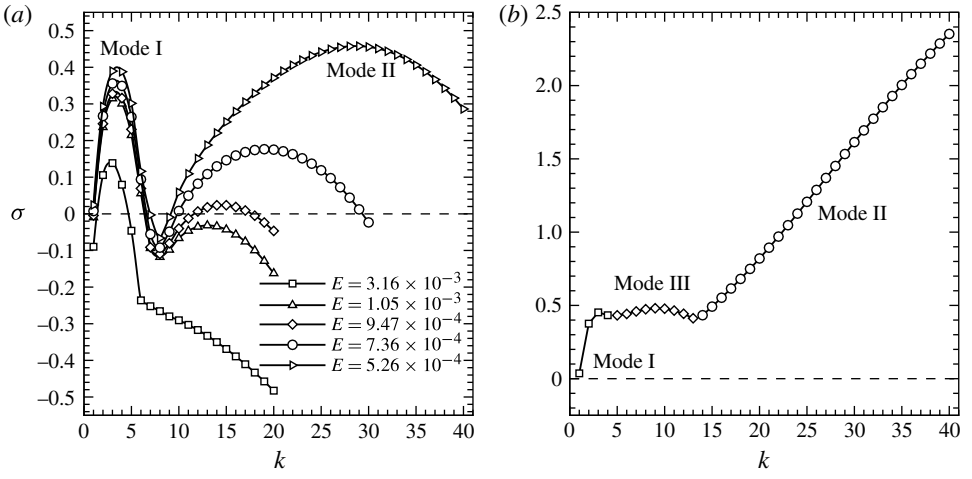


FIGURE 9. Growth rate σ as a function of wavenumber k for (a) various E at $Ro = 0.395$ and (b) $(Ro, E) = (0.5, 3 \times 10^{-4})$. Two mode peaks of σ are present at low and high wavenumbers denoted by mode I and II, respectively in panel (a). A third mode peak, mode III, is illustrated in panel (b). The dashed line represents the zero line where points above and below symbolize stable and unstable modes, respectively.

dimensional in the vertical. This is reflective of small-Ro and high-E flows, which is in agreement with the trends seen on growth rate against wavenumber plots. Thus, depth-independent contours of axial vorticity usually demonstrate dominance of mode I. Ascendency of mode II is characterized by the elongation of the negative-vorticity strands and the breaking of axial invariance in the base flow. Further elongation and development of the 'hooks' at the tip of the vorticity strands is associated with the emergence of mode III. It may be possible for mode III to become the most dominant by further increasing Ro or decreasing E, though this has not been observed in our parameter space.

5.1.2. *Global instability mode shapes*

The three-dimensional perturbation fields have also demonstrated axial invariance similar to its base flow counterpart for small-Ro flows. Axial vorticity contours of the $k_{peak} = 6$ perturbation associated with conditions of $Ro = 0.05$ and $E = 2 \times 10^{-4}$ are illustrated in figure 10. A pair of vertical vorticity strands are clearly shown around $r = 1$, which extends throughout the depth of the flow. In the faster-rotating region ($r < 1$), positive axial vorticity is generated, while its opposite is seen in the slower-rotating region ($r > 1$). It is also noted that the pair of vorticity strands is joined together closely all the way along the disk–tank interface. The pair is surrounded by weaker positive vorticity.

The joining of the positive- and negative-vorticity strands is divided at higher-Ro flows. An example of this is illustrated in figure 11, where a gap of fluid with an axial vorticity value similar to that of the surrounding flow is seen in between the pair of vorticity strands. Figure 11(a,b) presents the three-dimensional perturbation fields of mode I and II, respectively. Even when the base flow is no longer depth-independent, the unstable wavenumbers stemming from mode I still exhibit two strands of negative and positive perturbed vorticity. These strands encompass a region of positive axial vorticity, with the end of the strands connecting at the horizontal boundaries.

https://doi.org/10.1017/jfm.2013.594 Published online by Cambridge University Press

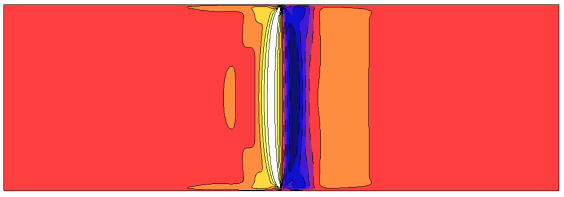


FIGURE 10. (Colour online) Contours of axial vorticity of the three-dimensional perturbation field of $Ro = 0.05$ for $E = 2 \times 10^{-4}$ depicted on the r–z plane. The most unstable azimuthal wavenumber $k = 6$ is shown here. Given the arbitrary scaling of linearized eigenvector fields, equi-spaced contour levels are plotted between $\pm(|\omega_{z,min}| + |\omega_{z,max}|)/2$. Dark (blue online) and light (yellow online) flooded contours represent negative and positive values, along with dashed and solid contour lines, respectively.

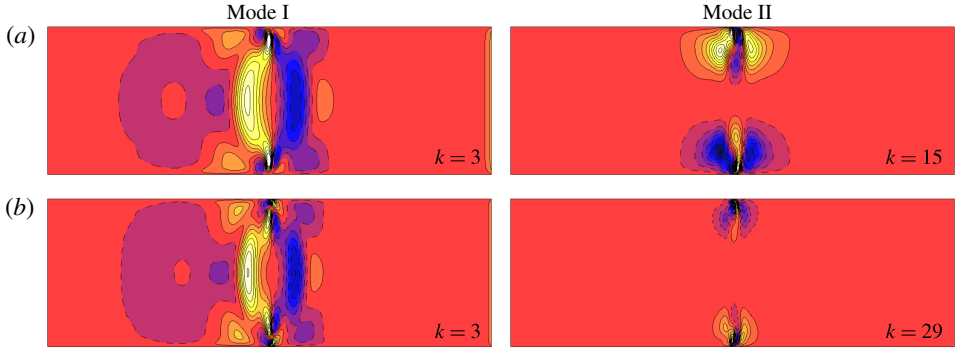


FIGURE 11. (Colour online) Contours of axial vorticity of the three-dimensional perturbation field of a given azimuthal wavenumber depicted on the r–z plane. The left and right columns illustrate the most unstable wavenumber from mode I and II peaks, respectively. The perturbation fields are obtained at $Ro = 0.395$ for (a) $E = 9.47 \times 10^{-4}$ and (b) $E = 5.26 \times 10^{-4}$. Contour levels are as per figure 10.

Perturbation fields belonging to mode II display highly localized disturbances around the periphery of the ring. On each disk, a negative- and positive-vorticity strand is sandwiched between contrasting vorticity patches. The strands do not extend into the interior to connect with the disturbances from the opposite disk. As such, mode II does not appear to be consistent with a barotropic instability. This is expected, as the growth of the mode II instability only appears when depth independence of the base flow is broken. The structures of the mode I and mode II instabilities do not differ significantly in these figures even though the flows are dominated by different instabilities. The similarity arises from the comparable growth rates between k_{peak} of modes I and II in figure 11(b).

When growth rates of wavenumbers from mode II are orders of magnitude greater than those of mode I, the structure of the perturbation field is altered. The perturbation fields are shown in figure 12. For the mode I waveband, the vorticity strands, which would otherwise extend over the entire depth, become truncated and extend diagonally into the interior. A similar trend is shown in the vorticity contours observed in the base flows (see figure 3b ii). However, a coupling of both positive- and negative-vorticity strands stems from $r = 1$. For the mode II waveband, the instabilities are

https://doi.org/10.1017/jfm.2013.594 Published online by Cambridge University Press

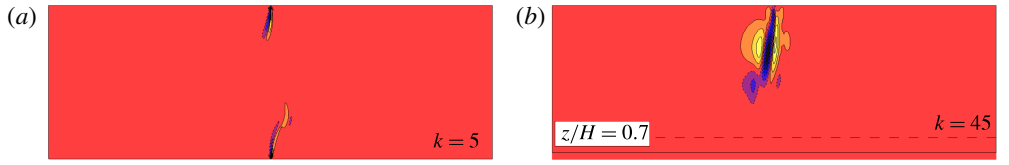


FIGURE 12. (Colour online) Contours of axial vorticity of the three-dimensional perturbation field of a given azimuthal wavenumber depicted on the r–z plane. Perturbation fields of the most unstable wavenumbers from (*a*) mode I and (*b*) mode II for conditions of $(Ro, E) = (0.273, 5.45 \times 10^{-5})$. The mode II disturbances are localized at the top horizontal boundary in this flow, and only the domain of $0.65 \leqslant r \leqslant 1.35$ and $0.65 \leqslant z/H \leqslant 1$ is shown. The dashed line represents a depth level of $z/H = 0.7$. Contour levels are as per figure 10.

only encouraged to grow at the top disk–tank interface (note that mode II in figure 12 only represents a third of the flow depth). No structures are evident in the interior or bottom of the flow. It is not clear why instabilities are favoured at the top boundary and suppressed at the bottom horizontal boundary.

In the event of the mode III instability emerging and overtaking the mode I, axial vorticity in the perturbation field exhibits both signed vorticity strands arising at $r = 1$ from the top and bottom boundaries, and extending all the way into the interior. However, the interior does not feature a clear depth-independent zone, instead adopting a complex structure comprising an amalgamation of negative and positive vorticity. These characteristics are not illustrated here.

5.1.3. *Visualizing the linear instability modes on horizontal planes*

In order to visualize the non-axisymmetric structure of the predicted linear instability modes, the leading eigenmodes are superimposed onto their respective axisymmetric base flow fields. Slices are then extracted in the r–θ plane for visualization in a top-down sense. These slices do not depict the actual three-dimensional flow structure that would be observed in an experiment, as nonlinear effects during the growth of the instability are bound to alter the flow structure. Rather, these fields demonstrate the type of distortions that these linear instabilities can induce on the axisymmetric base flow. Furthermore, we stress the fact that we only superimpose onto the axisymmetric state the leading instability eigenmode. In a real-case situation, a growing perturbation is likely to include a combination of several eigenmodes. The base flow and most unstable perturbation field (shown in figure 10) of $Ro = 0.05$ and $E = 2 \times 10^{-4}$ have been superimposed to generate figure 13. This process can be thought of as flows in which the linear instabilities have grown to finite amplitudes (though nonlinear effects are disregarded). This flow condition has only the mode I linear instability associated with it (figure 8). The mode I instability exhibits an axial vorticity field, which features a regular central polygon coupled with a strand of lower vorticity around the polygon border. The border is located approximately at the disk–tank interface. Here, the wavenumber 6 instability is represented by an interior hexagon of high vorticity, which is surrounded by lower vorticity around the perimeter. This strand of lower vorticity is thin, with its borders forming a hexagonal shape. Outside of this hexagonal structure, there are intermediate levels of vorticity attributed from the rotation of the tank (base flow). A ring of satellite vorticity patches *in lieu* of a thin strand around the interior polygon may be observed if the amplitude of the perturbation field is large compared to the amplitude of the base flow prior to the superposition.

https://doi.org/10.1017/jfm.2013.594 Published online by Cambridge University Press

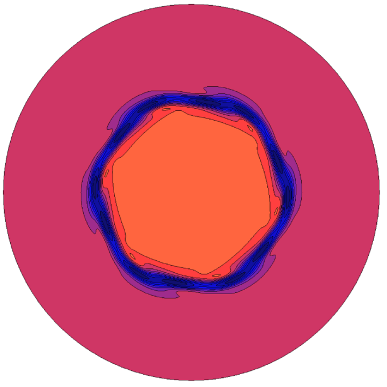


FIGURE 13. (Colour online) An r–θ slice taken at mid-depth in z is extracted from a linear non-axisymmetric flow approximation constructed by superposing the axisymmetric base flow and the leading instability mode with azimuthal wavenumber 6. This flow field is not representative of the three-dimensional non-axisymmetric flow since nonlinear effects are omitted here. The case shown had $Ro = 0.05$ and $E = 2 \times 10^{-4}$. Contours of axial vorticity are plotted, with levels as per figure 3. The orientation is such that the positive Ro causes the central region to rotate *clockwise* faster than the outer region.

Several more resultant flows from superimposing the perturbation fields with their respective flows are shown in figure 14. The perturbation fields correspond to those illustrated in figure 11. For wavenumbers belonging to mode II, the central vortex is circular in shape and is surrounded by a ring of vorticity patches near the horizontal boundaries, where the number of vortices corresponds to the wavenumber of the instability. The mid-plane does not exhibit any noticeable disturbances. With increasing wavenumber, the size of the vortices decreases in order to fit into the circumference at $r = 1$.

5.1.4. *Preferred azimuthal wavenumbers*

The most unstable wavenumbers for various Ro and E pairings have been mapped onto an Ro–E regime diagram. The resultant regime diagram is shown in figure 15. Fractional peak wavenumbers and corresponding peak growth rates were obtained via the local maximum of a parabolic fitting of the peak and the adjacent wavenumbers from the σ–k data obtained via linear stability analysis. These data points were used to generate a contour map of preferred wavenumber (for mode I) over the Ro–E space, allowing an accurate depiction of wavenumber segregation. As a result of using fractional peak wavenumbers, the wavenumber in the regime diagram represents a range of wavenumbers. For example, the contour band of 5 on the regime diagram represents the most unstable wavenumbers from $4.5 \leqslant k < 5.5$. Only peak wavenumbers from the mode I instability have been used to construct this regime diagram, even if wavenumbers from other mode peaks have higher growth rates. The purpose of this is to illustrate the preferential wavenumbers attributed by barotropic instability for specific flow conditions. The map depicts a decrease in unstable wavenumber with increasing E at lower Ro. At higher Ro, the dependence of unstable wavenumber shifts towards Ro, with wavenumbers decreasing with increasing Ro. These trends differ from those obtained experimentally. In Früh & Read (1999) their experimental trends depict a stronger dependence on Ro compared to E. The general trend is that either increasing Ro or decreasing E leads to a decreasing

https://doi.org/10.1017/jfm.2013.594 Published online by Cambridge University Press

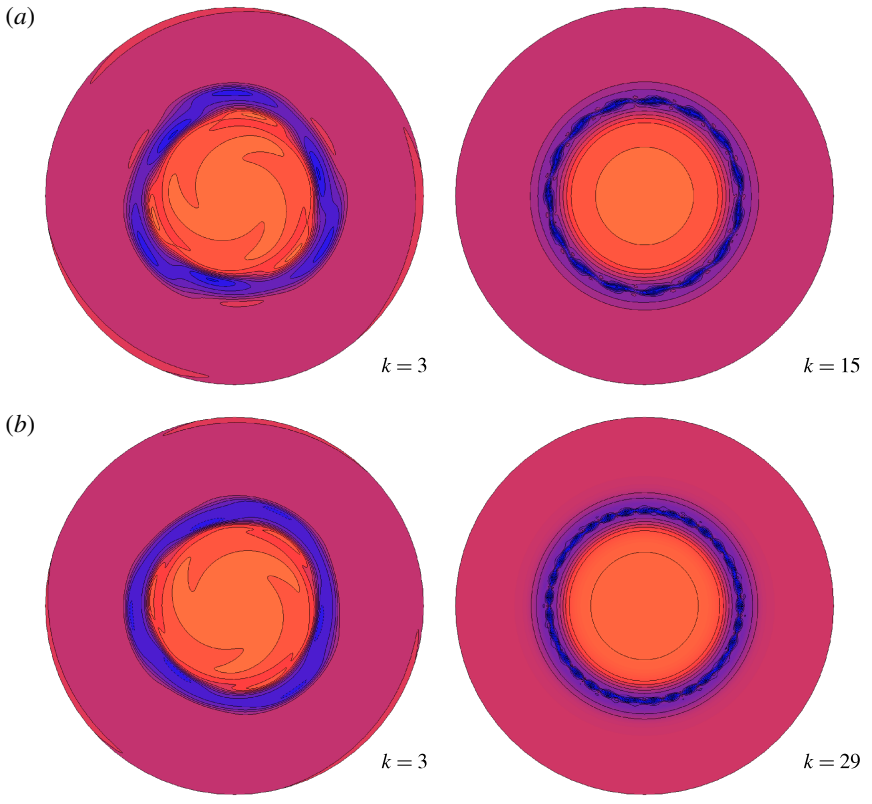


FIGURE 14. (Colour online) Slices of non-axisymmetric flows constructed by superposition of the base flow and the linear instability mode as per figure 13. These flow fields are not representative of the three-dimensional non-axisymmetric flow since nonlinear effects are omitted here. These cases show $Ro = 0.395$ at Ekman numbers (*a*) $E = 9.47 \times 10^{-4}$ and (*b*) $E = 5.26 \times 10^{-4}$. Left: the mode I instability is visualized on a slice extracted at mid-depth ($z/H = 0.5$). Right: the mode II instability is shown at $z/H = 0.85$ (near the top of the container). These cases correspond to the meridional semi-plane views of the perturbation fields from figure 11. Contour levels are as per figure 3 and the sense of rotation is as per figure 13.

wavenumber state. These trends were also observed by Aguiar *et al.* (2010) using differential rings instead of disks.

The dominance of either a mode I or II for each flow has also been mapped onto an *Ro*–*E* parameter space (not shown here). The transition between unstable wavenumbers belonging to mode I and mode II has been designated by a visually fitted line. This instability mode type threshold line is drawn on the regime diagram in figure 15 as a thick dashed line. This threshold is given by $Ro_{\mathrm{I-II}} = 5.44E^{0.35}$. In addition, the 'highly irregular' and 'period-doubled' threshold flow regimes from Früh & Read (1999) are overlaid on the regime diagram as black regions and a solid line, respectively. The overlap between the mode II instability found numerically and the time-dependent flows observed experimentally suggests that flows with a mode II dominance may be promoting this time dependence. Although the mode I–II threshold differs in exponent from the experimental non-modal flows, all of these flow regimes are seen to occur at higher *Ro* and lower *E*. In the same region of the parameter space,

https://doi.org/10.1017/jfm.2013.594 Published online by Cambridge University Press

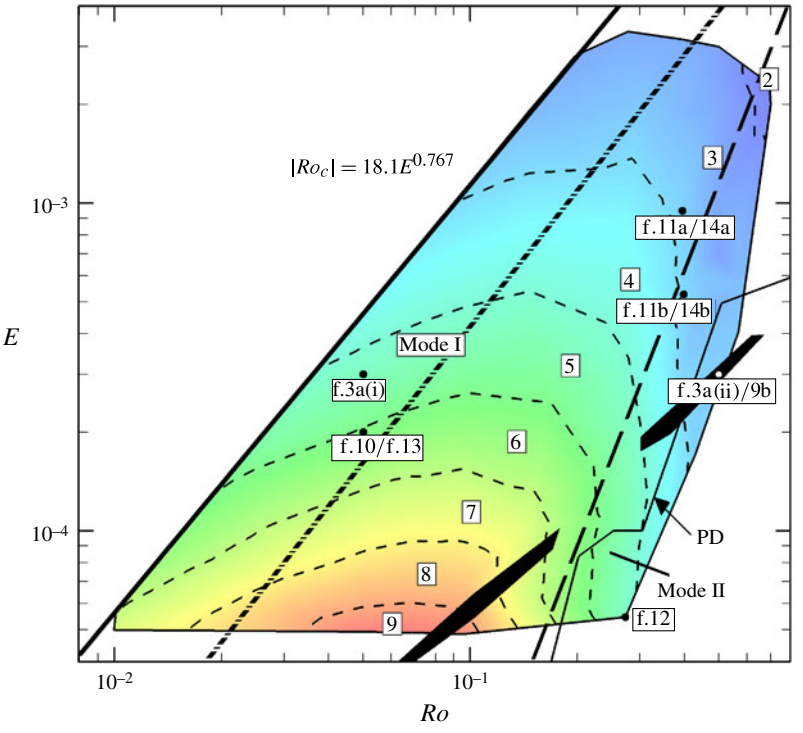


FIGURE 15. (Colour online) The regime diagram of the most unstable linear wavenumber as a function of E and positive Ro. The short-dashed lines represent the transition between one wavenumber and another, denoted by the wavenumber of the instability shown within the band. The solid boundary lines represents the range of triangulation. The left thick boundary line represents the stability threshold, which is given by $Ro_c \propto E^{0.767}$ (using positive- and negative-Ro data). The thick dashed line is a visual fit, separating flow conditions that are mode I and II dominant dictated by $Ro_{\mathrm{I-II}} \propto E^{0.35}$. The PD line and black regions are extracted from Früh & Read (1999) and represent period-doubled solutions and highly irregular flow, respectively. The dash-dotted line represents the stability threshold obtained by Früh & Read (1999), given by $|Ro_c| = 27E^{0.72}$. Black circles and the adjacent labels denoted by f.x mark the flow conditions illustrated in the respective figure x.

Aguiar *et al.* (2010) also found time-dependent flows, which they denote as 'chaotic' flows. Alternatively, it is possible that nonlinear effects in real experiments alter the regime diagram, a subject that will be addressed in future numerical work.

The empirical relationship of the critical Rossby number as a function of Ekman number found by Früh & Read (1999) is given by $|Ro_c| \approx 27E^{0.72}$. This relationship was obtained using both positive and negative data points, as the experimental study found little differences between positive and negative Ro_c. This similarity was predicted by the asymptotic analysis conducted by Busse (1968), who found that $|Ro_c|$ scales with $E^{3/4}$. The numerical investigation here yields the threshold of stability to be $Ro_c = 16.877E^{0.758}$ when considering positive-Ro data only. The threshold equation is given by $|Ro_c| = 18.11E^{0.767}$ when using both positive- and negative-Ro data. It should also be noted that the threshold obtained by Hide & Titman (1967) of $|Ro_c| = 16.8E^{0.568}$ is shifted even further to the right with a differing slope (not shown in the regime diagram).

https://doi.org/10.1017/jfm.2013.594 Published online by Cambridge University Press

There is a quantitative mismatch in the leading coefficient between the numerical result and the experimental empirical fit, although the exponent of E is in good agreement, both to the asymptotic result of 3/4 (Busse 1968) and to experimental results suggesting a 0.72 scaling. The higher coefficient causes a horizontal shift of the threshold line towards higher Ro, given that the exponent is similar. This can be seen in figure 15 between the solid line (numerical) and the dash-dotted line (experimental). The horizontal shifting to the right may be due to difficulty detecting instabilities at very small amplitudes due to limitations of the experimental measurements. This is revisited later in § 5.3. The numerical linear stability analysis conducted is able to pinpoint the stability threshold via the growth rate but does not include any information about the saturated amplitudes of the instabilities. However, it is expected that the structures are weak slightly beyond the onset of the stability threshold. The difference in coefficients causes a significant difference in the critical internal Reynolds number (equaton (3.4)).

To summarize, the differences in preferential wavenumber trends between numerical and laboratory results may be attributed to geometric differences, nonlinear effects, experimental observation and measurement techniques, and time dependence of flow states. The centre of the tank used in the laboratory contains a vertical rod used to drive the two horizontal disks. The addition of this rod may introduce perturbations into the flow that interact with the unstable shear layers and therefore alter the stability. A type of vortex shedding was observed from the central rod in simulations conducted by Bergeron *et al.* (2000) and Früh & Nielsen (2003). Nonlinear effects may also encourage competition between instability modes that cause the flow to undergo various wavenumber transitions. During this process, hysteresis effects are present, and therefore the resulting structure is highly dependent on the flow's history. In addition, the sharp changes in the contour lines of figure 15 are due to a number of factors, including the scatter of the data points used to construct the map and the method used to determine the peak wavenumbers. A parabolic fitting of the three closest points to the local peak in the σ–k data is used to determine the true peak growth rate and wavenumbers. Preferential wavenumbers associated with mode I were obtained for more than 100 different positive-Ro flow conditions, which is used to construct the positive Ro–E regime diagram.

5.2. *Negative Rossby numbers*

5.2.1. *Growth rates*

A stability analysis was conducted on negatively forced flows in a similar fashion to that conducted for the positive-Ro regime. Many similarities were observed and will be briefly noted, but emphasis will be placed on distinct features of the negative-Ro regime that distinguish it from the positive-Ro regime. Unstable wavenumbers ranging from 3 to 13 were observed for the range of $Ro \geqslant -4.0$. This implies that negative-Ro flows are more sensitive to higher wavenumbers compared to positive-Ro flows. In comparison, experimental observations obtained azimuthal wavenumbers ranging from 2 to 8 for $Ro > -0.4$ (Früh & Read 1999).

As observed in the results of negative-Ro base flows, a larger range of Ro demonstrates axial symmetry. Thus, it is expected that the mode I instability will dominate a large parameter space in this negative regime. Mode II is also expected to arise, as depth-dependent flow was observed for $Ro < -1/A$. Similar to the positive regime, the breaking of depth dependence is a function of both Ro and E. Thus, counter-rotating flows are not expected to become mode II dominant instantly at $Ro = -1/A$.

https://doi.org/10.1017/jfm.2013.594 Published online by Cambridge University Press

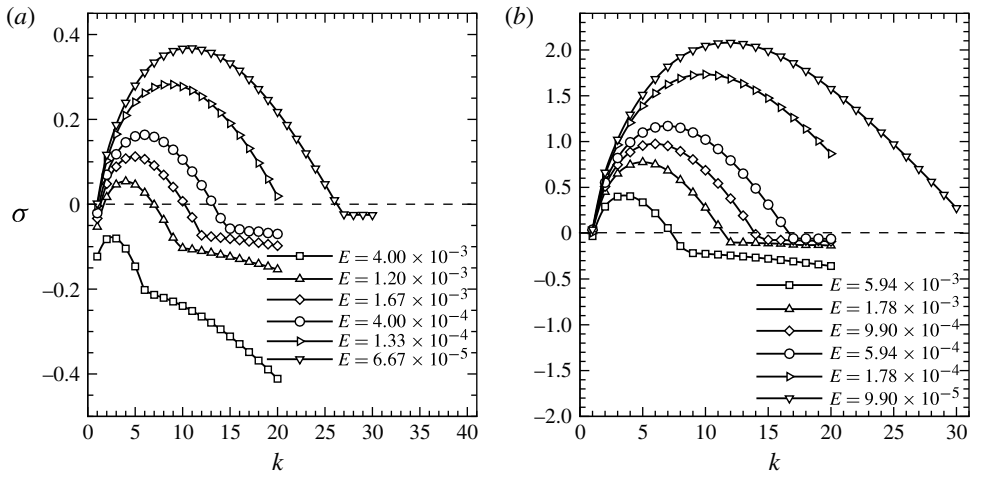


FIGURE 16. Growth rate σ as a function of wavenumber k for various E at (a) $Ro = -0.167$ and (b) $Ro = -1.46$. One maximum is seen for each E case. The dashed line represents the zero line where points above and below symbolize stable and unstable modes, respectively.

Growth rates of wavenumbers beyond the mode I branch illustrate a gradual decrease like that of positive-Ro flows. These features are illustrated in figure 16 for two different Ro values. At a small $Ro = -0.167$ and a high $E = 4 \times 10^{-4}$, the flow is linearly stable. As E decreases, the growth rates increase and the peak wavenumber shifts to higher wavenumbers as well as increasing the bandwidth of unstable wavenumbers. The shift in peak wavenumber with decreasing E is much more evident in the negative-Ro regime compared to the positive-Ro regime. As the base flows for the majority of the negative-Ro regime explored do not break its depth independence, this mode peak is reflective of the barotropicity of the flow. That is, this peak is representative of the mode I instability found in the positive-Ro regime, which was determined to be barotropic. This observation supports the hypothesis that the other mode peaks emerge due to the departure of highly vertical-independent motion. Growth rates of a higher magnitude at $Ro = -1.46$ (relative to the positive-Ro regime) shown in figure 16(b) demonstrate only the mode I instability even for small E. The growth rates associated with $k > 30$ have been obtained, although they are not shown here.

Linear stability analysis results for a constant $E = 2 \times 10^{-3}$ with varying Ro are illustrated in figure 17. Two maxima in the σ–k data are evident. At small Rossby numbers, only mode I is present, which is consistent with previous findings in the positive-Ro regime. For cases of $Ro \leqslant -1/A$, mode II becomes present and eventually dominates with sufficiently high $|Ro|$. This can be seen for $Ro = -3.0$ and $Ro = -4.0$. Negative Rossby numbers of a larger magnitude have not been investigated, so it is unknown whether additional instability modes exist (e.g. mode III).

5.2.2. *Linear instability modes and visualization on horizontal planes*

An illustration of the perturbation field structure is shown in figure 18(a) for $Ro = -0.167$ and $E = 4 \times 10^{-4}$, which was most unstable to a wavenumber $k = 6$ (figure 16a). This flow condition only has the mode I instability. The perturbations are largely vertical, with a pairing of positive and negative strands of vorticity. It should be noted that an r–z plane at an arbitrary angle θ is shown, and that may not

https://doi.org/10.1017/jfm.2013.594 Published online by Cambridge University Press

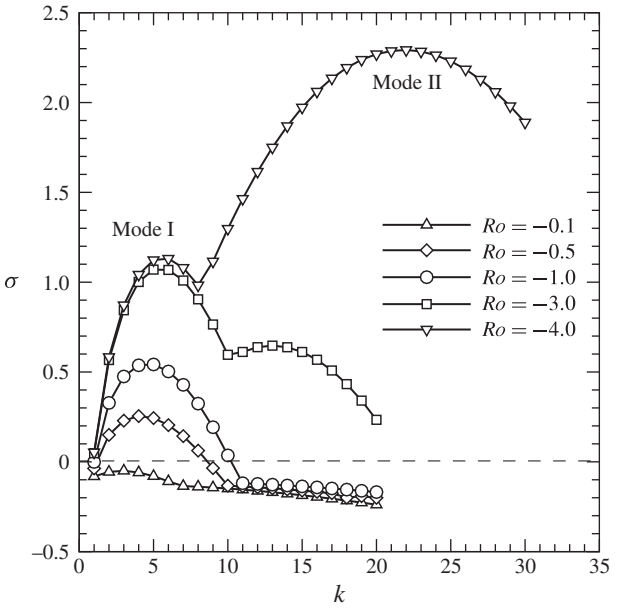


FIGURE 17. Growth rate σ as a function of wavenumber k for various Ro at $E = 2 \times 10^{-3}$. Mode I and mode II branches are present. The dashed line represents the zero line where points above and below symbolize stable and unstable modes, respectively.

represent flow structures at other azimuthal phase angles due to the non-axisymmetric mode structure. Further elucidation of the azimuthal mode structure is provided by superimposing this linear perturbation field onto the axisymmetric base flow (shown in figure 18*b*). Similar to figures 13 and 14, the purpose of this field is to demonstrate any flow alterations that occur as a result of the linear instability. A central hexagonal structure is present surrounded by six closed contours of vorticity. The ring of vorticity containing the six vorticity patches contains the highest vorticity in the flow. The lowest vorticity is situated in the central region.

The instability structures of modes I and II differ between positive- and negative-Ro regimes. Contour plots of axial vorticity in the perturbation fields for $Ro = -3.0$ and $E = 2 \times 10^{-3}$ are shown in figure 19. For mode I, a pair of positive and negative vertical vorticity strands still exist and remain bonded (even for $Ro = -4.0$). This is different from its positive counterpart, as a region of neutral vorticity grows between the strands with increasing Ro magnitude (figure 11). In addition to the vertical strands, there are positive vorticity strands angled towards the interior. The angle is similar to that observed in the base flow. The mode II structure also comprises a pair of positive and negative vorticity, except that it does not extend the entire depth and is localized to the horizontal boundaries. This localization was observed for positive-Ro flows also. These strands are also angled in a similar nature to that of mode I and the base flow (figure 3*b* ii).

5.2.3. *Preferred azimuthal wavenumbers*

Figure 20 shows the Ro–E regime diagram of the linearly unstable azimuthal wavenumbers for negative Ro. Like figure 15, this diagram is also constructed only from mode I wavenumbers, even if a flow is predicted to be dominated by a mode II linear instability. The figure presents an overview of the linear stability results and

https://doi.org/10.1017/jfm.2013.594 Published online by Cambridge University Press

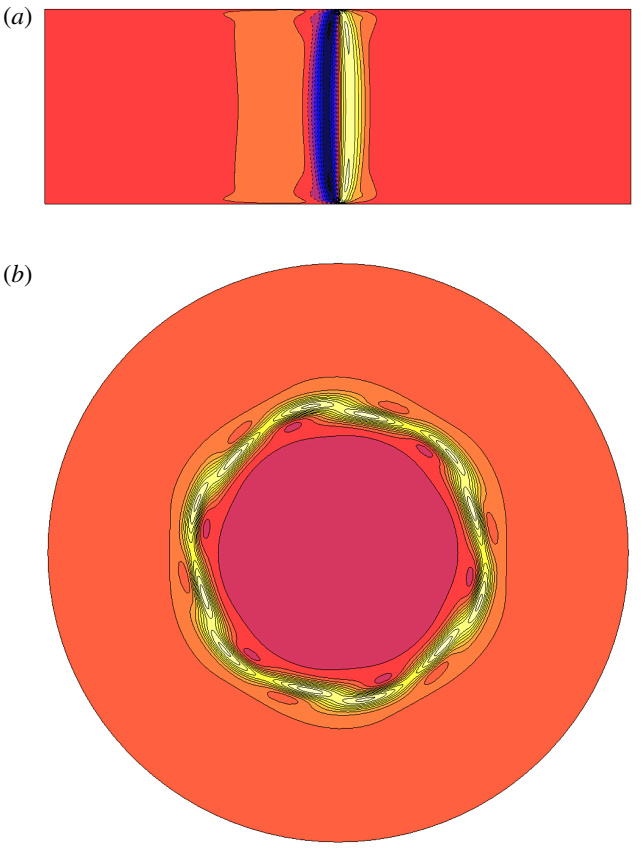


FIGURE 18. (Colour online) Axial vorticity contours of the dominant linear instability mode with azimuthal wavenumber $k = 6$ at $Ro = -0.167$ and $E = 4 \times 10^{-4}$. (*a*) The perturbation field of the instability mode is plotted in the z–r plane, with contour levels as per figure 10. (*b*) A linear non-axisymmetric flow constructed by superposing the axisymmetric base flow and the azimuthal linear instability wavenumber as per figure 13. This flow field is not representative of the three-dimensional non-axisymmetric flow since nonlinear effects are omitted here. The slice shown was extracted at mid-depth, with contour levels as per figure 3, and the orientation is such that the negative Ro causes the central region to rotate *anti-clockwise* faster than the outer region.

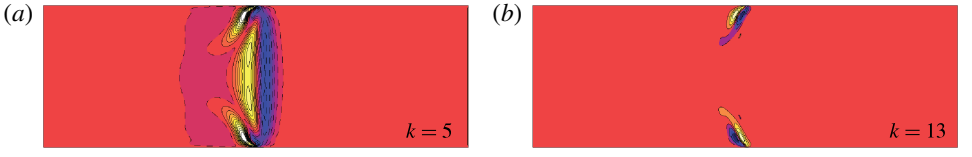


FIGURE 19. (Colour online) Contours of axial vorticity of the three-dimensional perturbation field of a given azimuthal wavenumber depicted on the r–z plane. Perturbation fields of the most unstable wavenumbers from (*a*) mode I and (*b*) mode II for conditions of $(Ro, E) = (-3.0, 2 \times 10^{-3})$. Contour levels are as per figure 10.

https://doi.org/10.1017/jfm.2013.594 Published online by Cambridge University Press

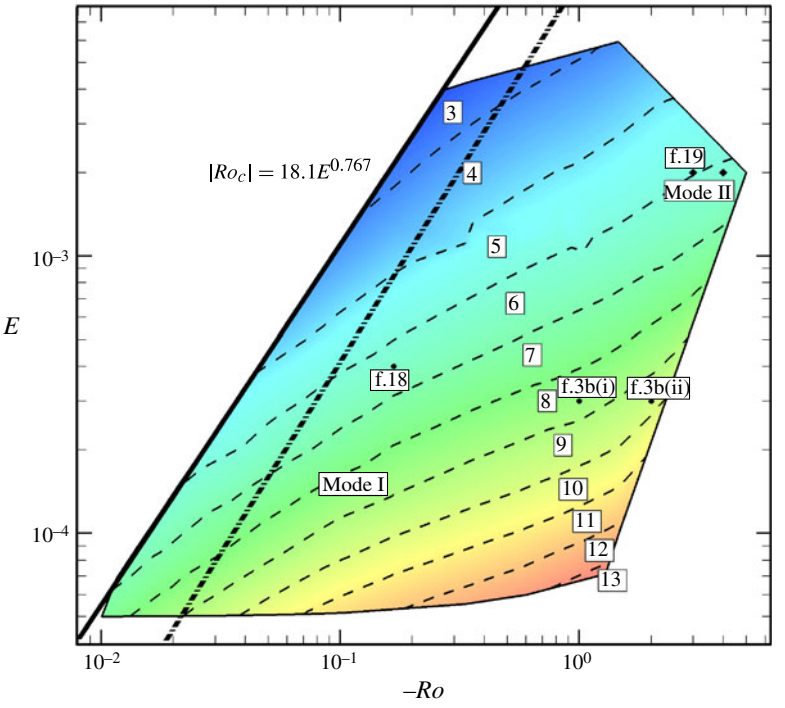


FIGURE 20. (Colour online) The same as figure 15 except for negative *Ro*. The black filled diamonds represent flow conditions that are mode II dominant.

suggests a decrease in unstable wavenumbers for decreasing *Ro* or increasing *E*. This is in contrast to the trend observed for the positive-*Ro* regime, where the preferential wavenumber is dependent on both *Ro* and *E* in specific regions. In considering just the mode I dominant region, the negative- and positive-*Ro* regimes are comparable. The unstable azimuthal wavenumbers have a greater dependence on *E* rather than *Ro*, with no shift in parameter dependence. If more data for negative-*Ro* flows dominated by mode II were obtained, it may indeed suggest a greater *Ro* dependence on preferential wavenumbers like that seen in the positive-*Ro* regime.

Building upon the earlier assumption that mode II instabilities promote time-dependent flows, this type of flow would not be observed unless the disks and tank were counter-rotating. However, experimental work by Früh & Read (1999) described irregular and period-doubled flows for flows with disks rotating slower than the tank (not shown in figure 20). Irregular flows were primarily located at very low values of $E < 5 \times 10^{-5}$. The flow conditions numerically investigated here do not cover this lower-*E* space, so no direct comparisons can be made. However, there are no signs in any of the σ–k data obtained in this study to indicate the presence of other mode instabilities. While the linear stability analysis conducted here implicitly considers only azimuthal Fourier modes, other instabilities such as Taylor vortices on the z–r plane would be observable in the axisymmetric base flows. No indications of such structures were observed in the simulations reported, despite being seen experimentally (Früh & Read 1999). Preferential wavenumbers associated with mode I were obtained for more than 100 different negative-*Ro* flow conditions, which is used to construct the negative *Ro*–*E* regime diagram.

https://doi.org/10.1017/jfm.2013.594 Published online by Cambridge University Press

Empirically fitting Ro and E data points corresponding to zero growth yields the relationship $|Ro_c| = 19.76E^{0.777}$ for negative-Ro data. Referring back to the asymptotic result of $|Ro_c| \propto E^{3/4}$ and the experimental result of $|Ro_c| \propto E^{0.72}$, the numerical relationship is quite similar. Again, the higher coefficient is due to the horizontal shifting of the threshold line towards higher Ro given that the exponent does not differ greatly. A possible explanation was given in the positive-Ro results section. Despite the difference in exponents of E for the instability threshold between positive- and negative-Ro regimes ($Ro_c = 16.877E^{0.758}$ and $|Ro_c| = 19.76E^{0.777}$, respectively), the lines are indistinguishable on the log–log plot. Therefore, a stability threshold has been determined that uses both positive- and negative-Ro data. This concept is supported by experiments of Hide & Titman (1967) and Früh & Read (1999), which found no differences in the onset of instability between positive- and negative-Ro flows. The threshold using both regimes is given by $|Ro_c| = 18.11E^{0.767}$. As can be seen in both regime diagrams (figures 15 and 20), this threshold line fits the positive- and negative-Ro data very well.

5.3. *Internal Reynolds number and characterization of preferred wavenumber regime diagrams*

The internal Reynolds number is known to play an important role in characterizing the stability of the Stewartson layers generated in this and similar previous studies. The various definitions of internal Reynolds number appearing in the literature share a common dependence between Rossby and Ekman numbers, namely $Ro/E^{3/4}$, differing only by constant factors arising from the choice of characteristic length and velocity scales (e.g. whether half or the full velocity differential across the shear layer, etc.). Unravelling the quoted critical internal Reynolds numbers from the literature shows a striking consistency. The theoretical analysis of Niino & Misawa (1984) yields a critical internal Reynolds number of 11.7, while from experiments van de Konijnenberg *et al.* (1999) determined $Re_{i,c} = 16.6$. The line of best fit that Früh & Read (1999) employed to determine a critical internal Reynolds number yielded approximately 24, though their figure 8 demonstrates that they found unstable flows down to $Re_i \approx 10.9$. The linear stability analysis conducted in this study returns a critical internal Reynolds number of 22.4 ± 0.8 across the considered range of Ekman numbers. However, dividing each of these values through by the respective prefactors to $Ro/E^{3/4}$ employed in each definition of Re_i yields the critical values listed in table 1. As can be seen, these show a remarkable consistency across the analytical, experimental and numerical methods employed in the studies, all producing a critical threshold within the range $15.4 < Ro/E^{3/4} < 16.6$. Note that the difference between the critical $Ro/E^{3/4} = 15.8$ and the coefficient of 18.1 in the Ro_c relationship (figures 15 and 20) is due to the difference in powers of Ekman number (namely $E^{3/4}$ and $E^{0.767}$ in the respective relations).

Revisiting figure 15 in the context of the importance of Re_i on the shear layer, it can be seen that the lines of constant preferred azimuthal wavenumber respond to changes in Re_i. For instance, the preferred wavenumbers exhibit a steady increase with increasing Reynolds number to $Re_i \approx 49$, beyond which the contours turn downwards. Eventually (beyond $Re_i \gtrsim 194$), the lines of constant azimuthal wavenumber are approximately vertical, demonstrating that the stability of the flow (at least in terms of the dominant azimuthal wavenumbers of the instabilities) is independent of Ekman number. Hence the flow can be divided into three regimes: $Re_i \lesssim 49$, for depth-independent (barotropic) flows; $49 \lesssim Re_i \lesssim 194$, representing a transitional zone;

https://doi.org/10.1017/jfm.2013.594 Published online by Cambridge University Press

Study	$Re_{i,c}$	$Re_{i,c}/(Ro/E^{3/4})$	Critical $Ro/E^{3/4}$
Niino & Misawa (1984)	11.7	$1/\sqrt{2}$	16.5
van de Konijnenberg *et al.* (1999)	16.6	1	16.6
Früh & Read (1999)	10.9 (lowest point)	$1/\sqrt{2}$	15.4
Present study	22.4 ± 0.8	$\sqrt{2}$	15.8 ± 0.57

TABLE 1. Critical internal Reynolds numbers quoted by various studies, the factors by which each definition of Re_i differ, and the corresponding critical value of $Ro/E^{3/4}$ found in each study.

and $Re_i \gtrsim 194$, an Ekman-number-independent regime. These are not precise threshold criteria; rather, they are determined approximately by inspection.

It turns out that the preferred wavenumbers obtained in the 'barotropic' positive-Ro regime for $Re_i \lesssim 49$ are consistent with those obtained in the negative-Ro regime (i.e. figure 20) if the data are plotted against $|Ro|$. This motivated a search for a grouping of $|Ro|$ and E that might universally collapse the data onto a single curve. Recasting the preferred azimuthal wavenumbers k as azimuthal wavelengths $\lambda_\theta = 2\pi/k$, an optimization procedure was used to maximize the correlation coefficient (r^2) of a power-law fit to the data when plotted against $|Ro|^\alpha E^\beta$, where exponents α and β were variables in the optimization process. A highly optimal pair of exponents giving a correlation coefficient $r^2 = 0.989$ was found to be $\alpha = 1$ and $\beta = -2$. Using $|Ro|/E^2$ as an independent variable, the universal power-law fit describing the preferred azimuthal wavelength of the mode I instability is given by

$$\lambda_\theta = 11.4(|Ro|/E^2)^{-0.167}, \tag{5.1}$$

and this universal fit is plotted in figure 21(*a*). Interestingly, the exponent in this expression is almost precisely $-1/6$, which if substituted produces $\lambda_\theta \sim E^{1/3}/|Ro|^{1/6}$ through a rearrangement of (5.1). Given the appearance of $E^{1/3}$ in this expression, it is highly likely that the instability wavelength scales with the $E^{1/3}$ Stewartson layer. This may have implications for the validity of quasi-geostrophic models of these flows, which do not capture the $E^{1/3}$ layer.

In the Ekman-number-independent stability regime, the preferred azimuthal wavelengths vary only with Rossby number. Our analysis determined that a convenient universal collapse of the data in this regime could be obtained by adopting ω/Ω as the independent variable. The resulting best fit of a power-law relationship to the data with $Re_i > 194$ was found to be

$$\lambda_\theta = 1.97(\omega/\Omega)^{0.497}, \tag{5.2}$$

which is plotted in figure 21(*b*). This fit achieved a correlation coefficient of $r^2 = 0.9764$. The 0.497 exponent is within 0.6 % of the exponent describing a square-root relationship. Therefore, in this regime it is proposed that the preferred azimuthal wavelengths follow $\lambda_\theta \sim \sqrt{\omega/\Omega}$.

It is stressed that the relationships developed here for the preferred azimuthal wavelengths of the shear-layer instability are based on a linear stability analysis of

https://doi.org/10.1017/jfm.2013.594 Published online by Cambridge University Press

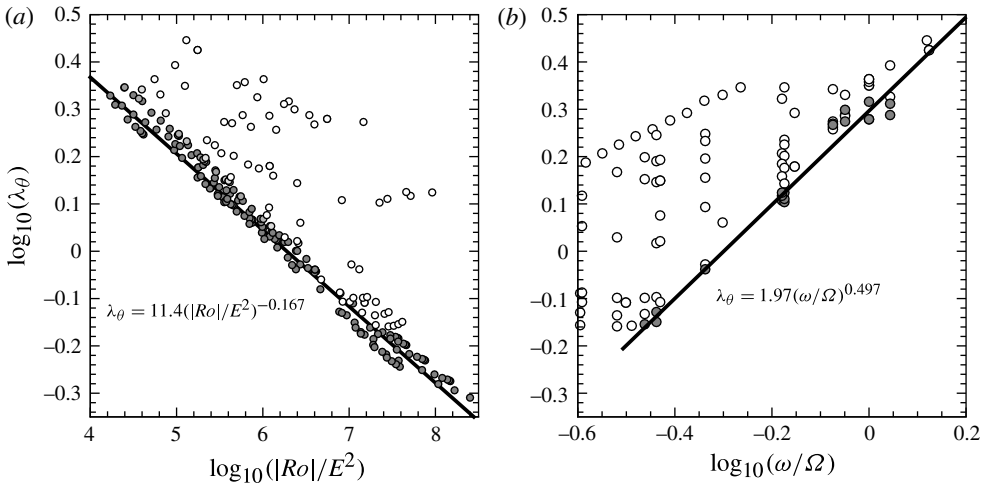


FIGURE 21. (Colour online) Regressions of the preferred azimuthal wavelength of the mode I instability. (*a*) Plot of $\log_{10}(\lambda_\theta)$ against $\log_{10}(|Ro|/E^2)$. The data are shaded by Re_i, with dark shading showing $Re_i \lesssim 49$. This captures the regime of depth-independent axisymmetric flows, and a linear collapse of the data is seen. (*b*) Plot of $\log_{10}(\lambda_\theta)$ against $\log_{10}(\omega/\Omega)$. Here dark shading identifies $Re_i \gtrsim 194$, which captures the regime of Ekman-number-independent instability wavelengths at high Ro and low E. The expressions obtained by least-squares power-law fitting to the data are included in each plot.

the axisymmetric shear-layer solutions. It is expected that nonlinear effects will play a role in modifying (reducing) the eventual azimuthal wavenumbers that would be seen in a physical experiment after the instability grows sufficiently to break into a ring of well-defined vortices (Früh & Read 1999; Aguiar 2008; Aguiar *et al.* 2010).

6. Conclusions

The structure of axisymmetric base flow of a rotating flow in a cylindrical container with differential rotation forcing at the boundaries and its linear stability has been investigated numerically. The dimensions of the numerical model are based on the laboratory apparatus used in Früh & Read (1999).

A variety of axisymmetric steady-state base flows were obtained, which are characterized by the governing parameters of Rossby and Ekman numbers. Results of both positive and negative forcing were obtained, with several distinct base flow features displayed. For small values of $|Ro|$, the flow remained highly two-dimensional following predictions from the Taylor–Proudman theorem. The depth-independent velocity and vorticity profiles were analysed to determine the relationships and thickness scalings of the Stewartson layers. The results agree well with theoretical predictions in the limit of small Ro. Universal relationships for $\delta/E^{1/3}$ and $\delta/E^{1/4}$ have been developed and demonstrate a linear dependence against ω/Ω for negative- and small-positive-Ro flows. As $|Ro|$ is increased, negative-vorticity strands are seen stemming from the disk–tank interface, which demonstrates a disruption to the two-dimensionality of the flow. This breaking of two-dimensionality occurs at a much lower $|Ro|$ for positive Ro compared to negative Ro. A possible explanation for this may be given by the sign of the axial vorticity generated at the disk–tank interface.

https://doi.org/10.1017/jfm.2013.594 Published online by Cambridge University Press

The breaking of the flow's axial invariance was seen to affect the nature of its linear stability. For base flows illustrating barotropic features, a single mode peak was present, which is associated with barotropic instability. When superimposed onto the base flow, the barotropic leading instability mode demonstrates vorticity forming polygonal structures such as triangles, pentagons and hexagons. The combination of several instability modes and nonlinear effects are likely to alter such linear patterns in real-world cases. A second and third mode peak were also observed at high Ro and low E, the same conditions where the depth independence of the base flow is broken. Modes II and III exhibited highly localized and irregular instabilities, respectively, which are atypical of barotropic instability. These instability modes also favoured higher wavenumbers. A compilation of the results corresponding to mode I were used to construct Ro–E regime diagrams.

The empirical relationship of the stability threshold for negative and positive Ro was obtained. Both were in good agreement with asymptotic predicted exponents obtained by Busse (1968), and little differences were observed between the threshold of positive- and negative-Ro flows. Consequently, the exponent for the relationship between $|Ro|$ and E correspond to a constant $|Re_i|$. Although the stability of the flow can be described by $|Re_{i,c}|$ alone, the preferential wavenumber state requires both $|Ro|$ and E to be known. Empirical fits of the preferential azimuthal wavenumber as functions of $|Ro|/E^2$ and ω/Ω have been determined for depth-independent ($Re_i \lesssim 49$) and depth-dependent ($Re_i \gtrsim 194$) flows, respectively.

In comparison to the stability threshold obtained by Früh & Read (1999), similarities were observed in the exponent, with differences seen in the leading coefficient. This is caused by the stability onset occurring at higher Ro values, and therefore at higher Re_i. This dissimilarity may be explained by experimental observation limitations. In addition, the discrepancy observed between the values of $Re_{i,c}$ determined in previous literature and this study is due to the different length and velocity scales used. Compensating for these differences, consistent threshold values of $15.4 \lesssim Ro/E^{3/4} \lesssim 16.6$ are found across the theoretical, laboratory and numerical studies of Niino & Misawa (1984), Früh & Read (1999), van de Konijnenberg *et al.* (1999) and the present simulations. The Ro–E regime diagrams depict a different trend from those obtained experimentally by Früh & Read (1999) and Aguiar *et al.* (2010). The primary reason for the differences in trends may be explained by the nonlinearity associated with these experimental flows. Future work will be devoted to study numerically nonlinear shear-layer instability, and to compare to results presented in this work.

The linear stability results of the Stewartson layer presented here suggest a potential for short-wavelength instabilities to exist near the end-plate interfaces for flow conditions beyond $Re_i \simeq 200$. Thus, the internal Re_i may be a critical parameter when designing configurations for the experiments in relation to solving the nonlinear stability of Keplerian flow. In addition, the E-independent thicknesses at high Re_i may provide a quantity for the number of split rings required.

Acknowledgements

T.V. received a PhD scholarship through the Faculty of Engineering, Monash University. This research is supported by the Australian Research Council through Discovery Grant DP120100153. Numerical work was made possible thanks to a high-performance computing grant from the National Computational Infrastructure (NCI), which is supported by the Australian Commonwealth Government. The computational

https://doi.org/10.1017/jfm.2013.594 Published online by Cambridge University Press

resources of the Monash SunGRID system through the Monash e-Research Centre were invaluable to the completion of this work. The authors thank the anonymous referees whose comments have helped to improve the quality of this paper.

REFERENCES

AGUIAR, A. C. B. 2008 Instabilities of a shear layer in a barotropic rotating fluid. PhD thesis, University of Oxford, UK.

AGUIAR, A. C. B. & READ, P. 2006 Instabilities of a barotropic shear layer in a rotating fluid: asymmetries with respect to sgn(*Ro*). *Meteorol. Z.* **15** (4), 417–422.

AGUIAR, A. C. B., READ, P. L., WORDSWORTH, R. D., SALTER, T. & YAMAZAKI, Y. H. 2010 A laboratory model of Saturn's north polar hexagon. *Icarus* **206** (2), 755–763.

AVILA, M. 2012 Stability and angular-momentum transport of fluid flows between corotating cylinders. *Phys. Rev. Lett.* **108** (12), 124501.

BAKER, D. J. 1967 Shear layers in a rotating fluid. *J. Fluid Mech.* **29** (1), 165–175.

BARKLEY, D. & HENDERSON, R. D. 1996 Three-dimensional Floquet stability analysis of the wake of a circular cylinder. *J. Fluid Mech.* **322**, 215–241.

BERGERON, K., COUTSIAS, E. A., LYNOV, J. P. & NIELSEN, A. H. 2000 Dynamical properties of forced shear layers in an annular geometry. *J. Fluid Mech.* **402** (1), 255–289.

BLACKBURN, H. M., MARQUES, F. & LOPEZ, J. M. 2005 Symmetry breaking of two-dimensional time-periodic wakes. *J. Fluid Mech.* **522**, 395–411.

BLACKBURN, H. M. & SHEARD, G. J. 2010 On quasiperiodic and subharmonic Floquet wake instabilities. *Phys. Fluids* **22**, 031701.

BLACKBURN, H. M. & SHERWIN, S. J. 2004 Formulation of a Galerkin spectral element–Fourier method for three-dimensional incompressible flows in cylindrical geometries. *J. Comput. Phys.* **197** (2), 759–778.

BUSSE, F. H. 1968 Shear flow instabilities in rotating systems. *J. Fluid Mech.* **33** (3), 577–589.

CHOMAZ, J. M., RABAUD, M., BASDEVANT, C. & COUDER, Y. 1988 Experimental and numerical investigation of a forced circular shear layer. *J. Fluid Mech.* **187**, 115–140.

COGAN, S. J., RYAN, K. & SHEARD, G. J. 2011 Symmetry breaking and instability mechanisms in medium depth torsionally driven open cylinder flows. *J. Fluid Mech.* **672**, 521–544.

DYUDINA, U. A., INGERSOLL, A. P., EWALD, S. P., VASAVADA, A. R., WEST, R. A., BAINES, K. H., MOMARY, T. W., DEL GENIO, A. D., BARBARA, J. M., PORCO, C. C., ACHTERBERG, R. K., FLASAR, F. M., SIMON-MILLER, A. A. & FLETCHER, L. N. 2009 Saturn's south polar vortex compared to other large vortices in the solar system. *Icarus* **202** (1), 240–248.

FLETCHER, L. N., IRWIN, P. G. J., ORTON, G. S., TEANBY, N. A., ACHTERBERG, R. K., BJORAKER, G. L., READ, P. L., SIMON-MILLER, A. A., HOWETT, C., DE KOK, R., BOWLES, N., CALCUTT, S. B., HESMAN, B. & FLASAR, F. M. 2008 Temperature and composition of Saturn's polar hot spots and hexagon. *Science* **319** (5859), 79–81.

FRÜH, W. G. & NIELSEN, A. H. 2003 On the origin of time-dependent behaviour in a barotropically unstable shear layer. *Nonlinear Process. Geophys.* **10** (3), 289–302.

FRÜH, W. G. & READ, P. L. 1999 Experiments on a barotropic rotating shear layer. Part 1. Instability and steady vortices. *J. Fluid Mech.* **383**, 143–173.

GILMAN, P. A. & FOX, P. A. 1997 Joint instability of latitudinal differential rotation and toroidal magnetic fields below the solar convection zone. *Astrophys. J.* **484** (1), 439–454.

GODFREY, D. A. 1988 A hexagonal feature around Saturn's north pole. *Icarus* **76**, 335–356.

HIDE, R. & TITMAN, C. W. 1967 Detached shear layers in a rotating fluid. *J. Fluid Mech.* **29** (1), 39–60.

HOLLERBACH, R. 2003 Instabilities of the Stewartson layer. Part 1. The dependence on the sign of *Ro*. *J. Fluid Mech.* **492**, 289–302.

HOLLERBACH, R. & FOURNIER, A. 2004 End-effects in rapidly rotating cylindrical Taylor–Couette flow. In *MHD Couette Flows: Experiments and Models* (ed. R. Rosner, G. Rüdiger & A. Bonanno), AIP Conference Proceedings, vol. 733, pp. 114–121.

https://doi.org/10.1017/jfm.2013.594 Published online by Cambridge University Press

JANSSON, T. R. N., HASPANG, M. P., JENSEN, K. H., HERSEN, P. & BOHR, T. 2006 Polygons on a rotating fluid surface. *Phys. Rev. Lett.* **96**, 174502.

JI, H., BURIN, M., SCHARTMAN, E. & GOODMAN, J. 2006 Hydrodynamic turbulence cannot transport angular momentum effectively in astrophysical disks. *Nature* **444** (7117), 343–346.

KARNIADAKIS, G. E., ISRAELI, M. & ORSZAG, S. A. 1991 High-order splitting methods for the incompressible Navier–Stokes equations. *J. Comput. Phys.* **97**, 414–443.

VAN DE KONIJNENBERG, J. A., NIELSEN, A. H., JUUL RASMUSSEN, J. & STENUM, B. 1999 Shear-flow instability in a rotating fluid. *J. Fluid Mech.* **387**, 177–204.

KOSSIN, J. P. & SCHUBERT, W. H. 2001 Mesovortices, polygonal flow patterns, and rapid pressure falls in hurricane-like vortices. *J. Atmos. Sci.* **58**, 2196–2209.

KOSSIN, J. P. & SCHUBERT, W. H. 2004 Mesovortices in hurricane Isabel. *Bull. Am. Meteorol. Soc.* **85** (2), 151–153.

KUO, H. 1949 Dynamic instability of two-dimensional nondivergent flow in a barotropic atmosphere. *J. Atmos. Sci.* **6**, 105–122.

LIMAYE, S. S., KOSSIN, J. P., ROZOFF, C., PICCIONI, G., TITOV, D. V. & MARKIEWICZ, W. J. 2009 Vortex circulation on Venus: dynamical similarities with terrestrial hurricanes. *Geophys. Res. Lett.* **36**, L04204.

LUZ, D., BERRY, D. L., PICCIONI, G., DROSSART, P., POLITI, R., WILSON, C. F., ERARD, S. & NUCCILLI, F. 2011 Venus's southern polar vortex reveals precessing circulation. *Science* **332** (6029), 577–580.

MONTABONE, L., WORDSWORTH, R., AGUIAR, A., JACOBY, T., READ, P. L., MCCLIMANS, T. & ELLINGSEN, I. 2010*a* Barotropic instability of planetary polar vortices: concept, experimental set-up and parameter space analysis. In *Proceedings of the HYDRALAB III Joint Transnational Access User Meeting, Hannover, February 2010*, pp. 135–138.

MONTABONE, L., WORDSWORTH, R., AGUIAR, A. C. B., JACOBY, T., MANFRIN, M., READ, P. L., CASTREJON-PITA, A., GOSTIAUX, L., SOMMERIA, J., VIBOUD, S. & DIDELLE, H. 2010*b* Barotropic instability of planetary polar vortices: CIV analysis of specific multi-lobed structures. In *Proceedings of the HYDRALAB III Joint Transnational Access User Meeting, Hannover, February 2010*, pp. 191–194.

MURRAY, B. C., WILDEY, R. L. & WESTPHAL, J. A. 1963 Infrared photometric mapping of Venus through the 8- to 14-micron atmospheric window. *J. Geophys. Res.* **68**, 4813–4818.

NIINO, H. & MISAWA, N. 1984 An experimental and theoretical study of barotropic instability. *J. Atmos. Sci.* **41** (12), 1992–2011.

PAOLETTI, M. S., VAN GILS, D. P. M., DUBRULLE, B., SUN, C., LOHSE, D. & LATHROP, D. P. 2012 Angular momentum transport and turbulence in laboratory models of Keplerian flows. *Astron. Astrophys.* **547**, A64.

PAOLETTI, M. S. & LATHROP, D. P. 2011 Angular momentum transport in turbulent flow between independently rotating cylinders. *Phys. Rev. Lett.* **106**, 024501.

PEDLOSKY, J. 1987 *Geophysical Fluid Dynamics*. Springer.

PERALTA, C., MELATOS, A., GIACOBELLO, M. & OOI, A. 2009 Superfluid spherical Couette flow. *J. Phys.: Conf. Ser.* **150**, 032081.

PICCIONI, G., DROSSART, P., SANCHEZ-LAVEGA, A., HUESO, R., TAYLOR, F. W., WILSON, C. F., GRASSI, D., ZASOVA, L., MORICONI, M. & ADRIANI, A. *et al.* 2007 South-polar features on Venus similar to those near the north pole. *Nature* **450** (7170), 637–640.

RAYLEIGH, LORD 1880 On the stability, or instability, of certain fluid motions. *Proc. Lond. Math. Soc.* **11**, 57–72.

SCHAEFFER, N. & CARDIN, P. 2005 Quasigeostrophic model of the instabilities of the Stewartson layer in flat and depth-varying containers. *Phys. Fluids* **17**, 104111.

SCHARTMAN, E., JI, H., BURIN, M. J. & GOODMAN, J. 2012 Stability of quasi-Keplerian shear flow in a laboratory experiment. *Astron. Astrophys.* **543**, A94.

SCHLICHTING, H. 1979 *Boundary-Layer Theory*. McGraw-Hill.

SHEARD, G. J. 2009 Flow dynamics and wall shear-stress variation in a fusiform aneurysm. *J. Engng Maths* **64** (4), 379–390.

SHEARD, G. J. 2011 Wake stability features behind a square cylinder: focus on small incidence angles. *J. Fluids Struct.* **27**, 734–742.

https://doi.org/10.1017/jfm.2013.594 Published online by Cambridge University Press

SHEARD, G. J. & RYAN, K. 2007 Pressure-driven flow past spheres moving in a circular tube. *J. Fluid Mech.* **592**, 233–262.

SHEARD, G. J., THOMPSON, M. C. & HOURIGAN, K. 2005 Subharmonic mechanism of the mode C instability. *Phys. Fluids* **17**, 111702.

SMITH, S. H. 1984 The development of nonlinearities in the $E^{1/3}$ Stewartson layer. *Q. J. Mech. Appl. Math.* **37** (1), 75–85.

SOLOMON, T. H., HOLLOWAY, W. J. & SWINNEY, H. L. 1993 Shear flow instabilities and Rossby waves in barotropic flow in a rotating annulus. *Phys. Fluids* A: *Fluid Dyn.* **5**, 1971–1971.

SOMMERIA, J., MEYERS, S. D. & SWINNEY, H. L. 1991 Experiments on vortices and Rossby waves in eastward and westward jets. *Nonlinear Topics Ocean Phys.* **109**, 227–269.

STEWARTSON, K. 1957 On almost rigid rotations. *J. Fluid Mech.* **3**, 17–26.

TAYLOR, F. W., DINER, D. J., ELSON, L. S., MCCLEESE, D. J., MARTONCHIK, J. V., DELDERFIELD, J., BRADLEY, S. P., SCHOFIELD, J. T., GILLE, J. C. & COFFEY, M. T. 1979 Temperature, cloud structure, and dynamics of Venus middle atmosphere by infrared remote sensing from Pioneer Orbiter. *Science* **205** (4401), 65–67.

VATISTAS, G. H. 1990 A note on liquid vortex sloshing and Kelvin's equilibria. *J. Fluid Mech.* **217** (1), 241–248.

VO, T., SHEARD, G. J. & MONTABONE, L. 2011 Stability of a rotating tank source–sink setup to model a polar vortex. In *Mechanical, Industrial, and Manufacturing Engineering* (ed. M. Ma), pp. 251–254. Information Engineering Research Institute.

VOOREN, A. I. 1992 The Stewartson layer of a rotating disk of finite radius. *J. Engng Math.* **26** (1), 131–152.

https://doi.org/10.1017/jfm.2013.594 Published online by Cambridge University Press